Eulerian and Lagrangian characterization of a high-amplitude convectively unstable shoaling internal solitary wave in two dimensions.

Tilemachos Bolioudakis

tb424@cornell.edu

Cornell University

Greg N. Thomsen

Wandering Wakhs Research

Peter J. Diamessis

Cornell University

Ren-Chieh Lien

University of Washington

Kevin G. Lamb

University of Waterloo

John Winnicki

Stanford University

Gustaaf Jacobs

San Diego State University

Research Article

Keywords: Internal Solitary Waves, Subsurface Core, Lagrangian Transport, Particle Tracking, Numerical Simulation

Posted Date: November 14th, 2025

DOI: https://doi.org/10.21203/rs.3.rs-7906656/v1

Additional Declarations: No competing interests reported.

Eulerian and Lagrangian Characterization of a High-Amplitude Convectively Unstable Shoaling Internal Solitary Wave in Two Dimensions

Tilemachos Bolioudakis[1*], Greg N. Thomsen[2], Peter J. Diamessis[1], Ren-Chieh Lien[3], Kevin G. Lamb[4], John Winnicki[5], Gustaaf Jacobs[6]

[1*]School of Civil and Environmental Engineering, Cornell University, Hollister Hall, Ithaca, 14850, NY, USA.
[2]Wandering Wakhs Research, USA.
[3]Applied Physics Laboratory, University of Washington, USA.
[4]Department of Applied Mathematics, University of Waterloo, Canada.
[5]Institute for Computational and Mathematical Engineering, Stanford University, USA.
[5]Department of Aerospace Engineering, San Diego State University, USA.

*Corresponding author(s). E-mail(s): tb424@cornell.edu;

Abstract

High-amplitude Internal Solitary Waves (ISWs), shoaling over a realistic transect of the gentle bathymetric slope in the South China Sea, are subject to subsurface convective instability ($\boldsymbol{U}_{\max} > \boldsymbol{C}$), which, in conjunction with the near-surface shear structure of the baroclinic background current, supports the development of a subsurface recirculating core. Through this core and its dynamic evolution, ISWs act as key drivers of material and mass transport. Via the one-way online coupling of a high-resolution, fully nonlinear non-hydrostatic flow solver integrated with a high-accuracy particle-tracking scheme, two-dimensional simulations of a single propagating ISW are conducted. The interaction between the formation and dynamic evolution of the ISW's convectively-driven recirculating core, its associated vortical structures, and the trajectories of neutrally

buoyant particles are examined. Particular emphasis is placed on identifying the primary entrainment pathway along a negative-vorticity layer at the rear of the ISW, as well as secondary entrainment routes subsequently emerging from the top and bottom of the core. In contrast, detrainment is found to occur primarily through a narrow channel in the ISW rear. These features are corroborated by Finite-Time Lyapunov Exponent (FTLE) analysis. The size and shape of the recirculating core are further examined using Lagrangian Coherent Structures (LCS), providing a complementary perspective to the classical Eulerian criterion based on $\boldsymbol{U}_{\max} > \boldsymbol{C}$. Finally, long-range particle transport and residence times are quantified, reaching $\boldsymbol{O}(\mathbf{10\ km})$ and durations on the order of hours, respectively, for a substantial fraction of entrained particles.

Keywords: Internal Solitary Waves, Subsurface Core, Lagrangian Transport, Particle Tracking, Numerical Simulation

1 Introduction

Internal solitary waves (ISWs) are nonlinear and non-hydrostatic phenomena that commonly arise in naturally stratified fluids. In the ocean, they have been frequently observed propagating over continental slopes and across various topographic features (Sandstrom and Elliott 1984; Klymak and Moum 2003; Scotti and Pineda 2004; Carter et al. 2005; Moum et al. 2003, 2007; Shroyer et al. 2011; Lien et al. 2005, 2012, 2014; Zhang and Alford 2015; Cheng et al. 2024). Isopycnal displacement of ISWs of depression up to 35% of the total water column depth has been observed. ISW's energy content originates at larger scales through inputs from tides and winds (Helfrich and Melville 2006; Stastna 2022), and can be carried for long distances before it is dissipated (Moum et al. 2003; St. Laurent 2008; Shroyer et al. 2010, 2011; Zulberti et al. 2020). ISWs preserve their coherent and symmetric waveform (Jackson et al. 2012), due to the balance between nonlinear steepening and physical dispersion. In addition, their rapid propagation speed, strong induced current velocity and induced shear, when interacting with background currents and oceanic bathymetry, can generate convective and shear instabilities within the water column (Lamb et al. 2019), enhancing strong turbulent mixing. Under favorable background vorticity conditions (He et al. 2019;

Rivera-Rosario et al. 2020), convective instability may also establish recirculating cores within ISWs, such that the water mass confined over a given volume persists inside the ISW over considerable distances (Lamb 1997, 2002, 2003; Lien et al. 2012).

ISWs are known to operate as efficient suppliers of nutrients into the upper ocean (Sandstrom and Elliott 1984; Reid et al. 2019) and affect the salt and mass exchange between the open ocean and coastal waters (Wang et al. 2007; Davis and Monismith 2011; Lucas and Pinkel 2022). Zhang and Alford (2015) report an estimate of ISW-driven cross-shore mass transport (average flux reported up to 0.38 $m^2 \cdot s^{-1}$) that is significant compared to the Ekman transport. The numerical study of Lamb (1997), and observations of Garwood et al. (2020), suggest that *nonbreaking* ISWs can be an important mechanism for horizontal particle transport. These studies further discuss the potential impact of ISWs on planktonic larval, postlarval invertebrates, and fish migration toward the shore. *Convectively* unstable ISWs are expected to exert a substantial influence on horizontal cross-shelf particulate transport and thereby significantly modulate marine ecology, compared to their stable counterparts (Lamb 2002). Observations of onshore transport of larvae and phytoplankton of Shanks et al. (2014), and horizontal mass transport of Lien et al. (2012) (rough estimate of approximately 18 Sv), are directly attributed to the action of internal waves with a convective instability-induced recirculating core.

As discussed in numerical simulations of convectively unstable, high-amplitude ISWs with subsurface cores (Rivera-Rosario et al. 2020, 2022), the entrained water mass typically consists of colder, denser fluid that enters the ISW core at a wave-amplitude-dependent critical depth, being deeper for larger waves. This cold water mass plunges into the wave interior, likely in the form of a turbulent gravity current (Bolioudakis et al. 2025), and is subsequently advected with the ISW while undergoing vigorous turbulent mixing. In the meantime, exchange of the entrained water with the surrounding environment is believed to occur through a "leaky" mechanism

associated with a trailing turbulent wake (Lamb 2002; Moum et al. 2003; Lien et al. 2012). The amplitude of the wave governs the intensity and extent of this wake, which tends to grow when shoaling upslope towards shallower waters and is associated with shear instabilities, often manifested as Kelvin-Helmholtz billows left behind the ISW (Bolioudakis et al. 2025). In the wake region, strong upwelling may bring aggregated biological material toward the surface (Moore and Lien 2007). In the northern South China Sea, pilot whales have been observed to follow ISWs, suggesting a potential link to enhanced prey availability in the wave's wake or "boil" (Moore and Lien 2007). Furthermore, ISWs are believed to ultimately disintegrate upon encountering sufficiently shallow topographic features, such as atolls and coral reef slopes, continental shelves, submarine ridges, shallow fjord sills and lakes, thereby releasing their entrained cold water in situ (Nielson and Henderson; Davis et al. 2020; Henderson 2016; Støylen and Weber 2010). This process could directly influence marine ecosystems, particularly coral reefs, by introducing temperature variability on daily or tidal timescales, conditions linked to potential reduction of coral bleaching risk (Safaie et al. 2018).

Accurately measuring transport induced by ISWs in the field remains highly challenging, as it requires non-trivial tracking and sampling of the wave interior with high spatiotemporal resolution. Lagrangian floats have been employed to observe internal waves, characterize their subsurface structure, and capture the associated turbulence (D'Asaro 2003; Lien et al. 2002; Girton et al. 2024). Although deploying instruments capable of capturing ISWs with recirculating cores is costly and technically demanding, measurements of internal waves and shear instability have been reported (Lien et al. 2002), demonstrating the utility of such measurements for monitoring turbulence and mixing. However, Lagrangian transport induced by internal waves has not yet been addressed. Due to inherent observational limitations and the transient nature

of ISWs, the link between subsurface instabilities and entrainment–detrainment processes remains unclear. In particular, the associated water-mass transformation and net transport driven by ISWs have yet to be quantified from in situ measurements.

Many previous studies have examined particle transport induced by internal waves using laboratory experiments (Umeyama and Matsuki 2011), as well as combined laboratory and numerical approaches (Luzzatto-Fegiz and Helfrich 2014; Deepwell et al. 2020). The associated transport of Mode-2 ISWs was discussed in the focused numerical study of Salloum et al. (2012). The dispersion of neutrally buoyant or passive tracer-like particles, those with negligible swimming capability, has also been explored through numerical simulations (Steinbuck et al. 2011; Stashchuk and Vlasenko 2021; Stastna et al. 2011), including analyses of their Lagrangian drift (Zhou and Diamessis 2015). Horizontal transport and drift induced by non-breaking ISWs have been investigated using heuristic models (Garwood et al. 2020) and fully nonlinear direct numerical simulations (Lamb 1997, 2002). Particle-tracking methods have further been employed to assess near-bottom transport generated by shoaling internal waves (Rouvinskaya et al. 2018), with particular focus on ISWs breaking over continental slopes (Arthur and Fringer 2016; Vieira and Allshouse 2020; Deepwell et al. 2020). With the exception of Guo et al. (2021), who utilized the MITgcm model at 75 m horizontal resolution to simulate three-dimensional shoaling ISW packets, most of the aforementioned studies have been limited to laboratory scales or focused on seafloor interactions involving particles and sediments. Building on earlier work on trapped-core-induced transport (Lamb 1997; Gil 2017) and the preliminary results of studies of lower-amplitude waves (not shown here), the present study investigates long-distance ($\mathcal{O}(10)$ km) transport of neutrally buoyant particles by a high-amplitude shoaling ISW with a recirculating core, along a realistic continental slope transect in the South China Sea (SCS).

To further characterize the underlying transport mechanisms and reveal coherent structures within the evolving particle field, one can employ a Lagrangian framework

based on Finite-Time Lyapunov Exponents (FTLE) to identify Lagrangian Coherent Structures (LCS). LCS derived from ridges of FTLE fields have become a widely adopted diagnostic tool for studying complex, time-dependent dynamical systems, particularly in geophysical and environmental flows (Haller 2002; Shadden et al. 2005; Haller 2015). Recent work by Zhang et al. (2024) analyzed the FTLE topology associated with a stably propagating laboratory-scale ISW in idealized two-dimensional simulations, while Vieira and Allshouse (2020) used spectral clustering to identify materially coherent vortices (termed boluses) as LCS in stably shoaling waves. In a related effort, Luzzatto-Fegiz and Helfrich (2014) applied FTLE-based LCS analysis to laboratory experiments of ISWs with trapped cores (referred to as "solicores") to estimate the core's spatial extent.

The high-amplitude ISWs observed in the SCS (Lien et al. 2012, 2014; Chang et al. 2021) likely occupy a distinctly different dynamical regime compared to the ISWs examined in previous studies. In particular, SCS ISWs are characterized by their ability to propagate over exceptionally long distances while shoaling toward the continental shelf, undergoing sustained interaction with variable bathymetry. During this prolonged shoaling, these waves frequently develop subsurface convective instabilities that give rise to large recirculating cores, defined as regions of closed streamlines in a frame of reference moving with the wave (Aigner et al. 1999; Lamb 2003), with vertical extents reaching up to 50 m. In field observations, zones where the total (including wave-induced and background components) horizontal velocity exceeds the wave celerity ($U_{\max} > C$) are commonly used as indicators of convectively unstable, trapped cores. Alternatively, Lagrangian diagnostics have proven effective in delineating the boundaries of these coherent wave structures (Luzzatto-Fegiz and Helfrich 2014), offering a more physically grounded and frame-independent criterion for identifying the formation and persistence of isolated recirculating regions.

High-resolution, fully nonlinear and non-hydrostatic two-dimensional (2D) simulations with Lagrangian particle tracking are performed here to investigate the evolution of a single, high-amplitude, convectively unstable ISW as it shoals over the gentle continental slope of the SCS. This study is motivated by the significance of shoreward transport of nutrients, marine microbiology and plankton driven by shoaling ISWs, particularly those supporting recirculating cores. The primary objective is to examine the formation of the ISW's recirculating core and to link its evolution to the entrainment and detrainment trajectories of neutrally buoyant particles. The size and structure of the recirculating core are also assessed from a Lagrangian perspective, in agreement with the corresponding Eulerian criterion of $U_{\max} \geq C$. Lastly, a long-range horizontal transport on the order of $\mathcal{O}(10)$ km is observed, associated with residence times on the order of 2-3 hours.

The paper is organized as follows. Section 2 outlines the simulation setup, including the oceanic region of interest, mathematical model, and computational domain. Section 3 presents the results of the particle-tracking simulations, focusing on the formation of the recirculating core and the development of vortical structures within the ISW interior. Particular attention is given to a distinct vorticity layer that extends from the core to the trailing edge of the wave, facilitating particulate exchange with the surrounding environment. Entrainment and detrainment processes are examined through selected particle trajectories and their velocity time series. The Eulerian $U_{\max}/C \geq 1$ criterion for identifying trapped cores is evaluated against LCS-based diagnostics, which provide a dynamically evolving characterization of core size and shape. Lagrangian transport and particle residence times are also assessed. Section 4 offers concluding remarks and discusses broader implications. Appendices provide additional details on the numerical tool and resources utilized (Appendix A) and the LCS computation methodology (Appendix B).

2 Method

2.1 Study Site and Background Conditions

The area of interest consists of the northern part of the SCS, which serves as an ideal natural laboratory for studying ISWs. High-amplitude ISWs are generated in a highly predictable manner from internal tides originating in the Luzon Strait. Although instability processes within these ISWs have been repeatedly observed, particularly during spring tides, spatiotemporal observational resolution has often been insufficient (Alford et al. 2015; Chang et al. 2021), especially when attempting to track the ISW and monitor its evolution across all three spatial dimensions. Following the approach of Rivera-Rosario et al. (2020, 2022); Bolioudakis et al. (2025), the present simulation focuses on an 80 km-long transect over a depth range of 365 to 921 m (shown in Fig. 1a). The bathymetric data used in the high-resolution simulations presented here are sampled from high-accuracy field measurements of Lien et al. (2005).

During the field measurements of Lien et al. (2014), two moorings were deployed near the steepest section of the aforementioned transect, and the subsurface recirculating core of a convectively unstable ISW was first detected at this location. Given that the formation of such a recirculating core requires a favorable sign of background vorticity (He et al. 2019), the time-averaged water column properties measured prior to the arrival of the first observed wave are used to define the background conditions in the present simulation. Specifically, the one-dimensional (i.e., depth-dependent) time-averaged horizontal current and density profiles serve as the ambient background fields (see Fig. 1b, which shows the Brunt-Väisälä (BV) frequency and the background current $U(z)$). Assuming ISWs propagation speeds comparable to those of the principal internal tide, background fields are held steady throughout the simulation, which spans less than 12 hours of physical time. Lastly, the location of the pycnocline is identified at a depth of $z_0 = 22\ m$, where the maximum BV frequency is observed. The

corresponding density at this depth, $\rho_0 = 1022.58\ kg \cdot m^{-3}$, is taken as the reference value.

2.2 Equations of Motion

The mathematical model employs the incompressible Euler equations under the Boussinesq approximation (IEEB). Following Rivera-Rosario et al. (2020), the effects of planetary rotation are neglected, as shoaling dynamics are expected to dominate (Lamb and Warn-Varnas 2015), particularly over the depth range characteristic of the study site. Furthermore, viscous and diffusive terms are neglected based on the assumption that the smallest resolved physical length scales (see Table 1) remain significantly larger than the Kolmogorov and Batchelor scales. Potential viscous effects near the seabed are also excluded from consideration, as they are assumed to have a negligible impact on the large-scale wave kinematics and flow structure within the region of interest. Under these assumptions, the governing equations of the two-dimensional motion are shown below, where $\hat{i}$ and $\hat{k}$ denote unit vectors pointing from left to right and from bottom to top respectively:

$$\frac{\partial \mathbf{u}}{\partial t} = -\mathbf{u} \cdot \nabla \mathbf{u} - U \frac{\partial}{\partial x}\mathbf{u} - w \frac{\partial U}{\partial z}\hat{i} - \frac{1}{\rho_0}\nabla p' - \frac{g}{\rho_0}\rho' \hat{k} \quad , \tag{1}$$

$$\frac{\partial \rho'}{\partial t} = -\mathbf{u} \cdot \nabla (\overline{\rho}(z) + \rho') \quad , \tag{2}$$

$$\nabla \cdot \mathbf{u} = 0 \quad , \tag{3}$$

In this 2D framework, the velocity vector $\mathbf{u}$ represents the wave-induced flow field within a Cartesian coordinate system, where x and z denote the horizontal and vertical directions, respectively. A steady background current, $U(z)$, oriented along the direction of wave propagation, is also included (see Fig. 1, panel b). The density field is decomposed into a constant reference value ρ_0, a steady background stratification

$\overline{\rho}(z)$ derived from in-situ measured water column profiles, and a perturbation component ρ' associated with the ISW and any finer-scale motions therein. In Eq. (1), the pressure perturbation p' includes the component related to the ISW-induced depression and associated finer-scale phenomena, and is defined relative to the background hydrostatic pressure distribution.

As a direct consequence of the inviscid and non-diffusive formulation of the governing equations, explicit boundary conditions are not imposed on the velocity and density fields (Bolioudakis et al. 2025). The pressure field, however, is subject to nonhomogeneous Neumann boundary conditions (Karniadakis et al. 1991).

2.3 Computational Domain

2.3.1 Spatial and Temporal Discretization Strategies

The 2D computational domain is shown in Fig. 1a), overlaid with $\sigma = \rho - 1000\,kg/m^3$ (hereafter referred to as density) contours, along with the initial ISW. The 80 km-long bathymetric transect corresponds to the high-accuracy field measurements of Lien et al. (2005), and has also been used in previous computational studies (Rivera-Rosario et al. 2020, 2022; Bolioudakis et al. 2025). An additional 20 km region of uniform depth is appended upstream of the transect (note the negative values along the horizontal axis in Fig. 1a). This artificial constant-depth region allows for smooth ISW propagation prior to shoaling, minimizing any spurious effects during the initialization phase.

The computational grid consists of spectral elements in both directions of the x–z plane (see Table 1). Within each element, the Gauss–Lobatto–Legendre (GLL) grid nodes are non-uniformly spaced (Canuto et al. 2007). The element sizes gradually decrease from the deeper to the shallower parts of the domain in both x and z. In the x-direction, horizontal element refinement is applied to resolve subsurface instabilities and wave breaking, while in the z-direction, vertical refinement reflects the decreasing

depth. Additional vertical clustering of elements is introduced around the depth range occupied by the waveform and wave interior, as indicated by the pycnocline depression, where instabilities are expected to develop during shoaling. As summarized in Table 1, the finest spatial resolution corresponds to grid spacings of $\Delta x_{\min} = 1.03\ m$ and $\Delta z_{\min} = 0.21\ m$.

The time-discretization scheme used in this study is described in Karniadakis et al. (1991); Diamantopoulos et al. (2022). The fixed time step is $\Delta t = 0.22\ s$, which satisfies the Courant–Friedrichs–Lewy (CFL) stability condition in both spatial directions, with a target CFL number of 0.5.

2.3.2 Overlapping windows

The computational domain is decomposed into successively overlapping horizontal subdomains, or *windows* (Rivera-Rosario et al. 2020; Diamantopoulos et al. 2022; Bolioudakis et al. 2025), with their respective right boundaries marked in Fig. 1a. Each of windows 3 to 9 spans approximately 12 wavelengths ($\lambda_w \approx 1\ km$), using 768 horizontal elements, with a six-wavelength overlap between successive windows. As the ISW approaches within three wavelengths of a window's right boundary, the simulation transitions to the next window, which extends the domain by six new wavelengths upslope. This process repeats itself until the ISW reaches the final domain boundary. This windowing strategy enables the efficient use of high along-wave spatial resolution within a limited portion of the domain, significantly reducing computational cost while preserving numerical accuracy throughout the shoaling process.

2.3.3 Wave characteristics

Table 1 summarizes the deep-water characteristics of the simulated ISW. The selected wave is the largest among the three ISWs considered in Bolioudakis et al. (2025), with a deep-water amplitude corresponding to a maximum isopycnal displacement of 150 m.

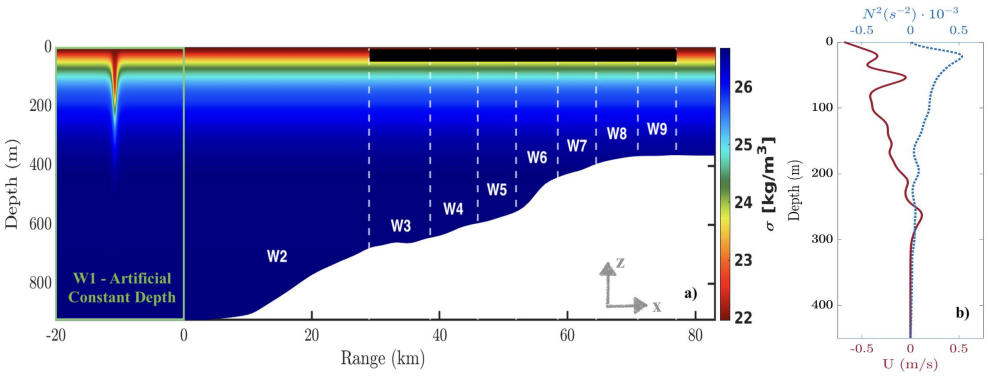

Fig. 1 Panel (a) shows the computational domain overlaid with density contours. The initial position of the ISW is marked, along with the right boundaries of the overlapping windows (white dashed lines), and the initial positions of the particles (black shaded region). Panel (b) displays the time-averaged background conditions: the horizontal current velocity profile (red curve) and the in-situ observed Brunt–Väisälä frequency profile (blue curve). These background fields are held fixed throughout the duration of the simulation.

We focus on this *150 m*-amplitude wave, which undergoes the most vigorous convective instability, and define the parameter space of our study as outlined in Sec. 2.4.

The initial two-dimensional ISW is computed as a solution to the fully nonlinear Dubreil–Jacotin–Long (DJL) equation (Long 1953; Turkington et al. 1991), using the pseudospectral method developed by Dunphy et al. (2011). This solution is obtained for the observed background conditions (see Fig. 1, panel b) and a prescribed target value of available potential energy. The wave generation procedure and the subsequent mapping onto the computational grid follows that of Rivera-Rosario et al. (2020); Bolioudakis et al. (2025).

2.4 Simulation Set-Up

In this study, two sets of 2D simulations are performed for the same propagating ISW. In both cases, the injected particles are non-buoyant, massless, and volume-less numerical markers, initialized at prescribed locations and subsequently advected by the model velocity field (i.e. idealized Lagrangian tracers; see van Sebille et al. (2018)). Since these particles exert no feedback on the flow, they serve solely as passive

Deep-Water Wave Properties		**Computational Domain**	
Amplitude (m)	150	Domain length (km)	80
Wavelength (m)	1010	Window length (km)	12
Propagation speed (m/s)	1.95	Depth range (m)	[365 921]
Spectral-Element Parameters		**Resolution and Time Step**	
Polynomial order	7	$\Delta x_{\min}$ (m)	1
Element count m_x	4202	$\Delta z_{\min}$ (m)	0.2
Element count m_z	60	Δt (s)	0.2

Table 1 The characteristics of the ISW at initialization, located over the deepest part of the transect, are summarized. The physical dimensions of the computational domain are provided, along with the spatial discretization parameters. The finest spatial resolution achieved in the simulation and the corresponding time-step value used are also indicated.

indicators of transport and stirring, and the ISW shoaling process remains identical in both simulations.

Simulation A

In this simulation, an initial cloud of 3306 particles is seeded within the ISW core when the wave centerline is located at 28 km along the domain. Specifically, these particles are injected at every grid point between $67-132$ m depth range, spanning a horizontal extent of 200 m centered around the wave centerline. Additional sets of particles are initialized within each overlapping computational window, positioned over the depth range occupied approximately by the pycnocline. Particles are seeded at every grid point within the x-range $29.5-76.5$ km and z-range 10 to 30 m, resulting in a total of 691,550 particles (see black shaded region of Fig. 1a). At each window transition, particles located within the overlapping region (see Sec. 2.3.2) are carried forward with the ISW solution into the subsequent window. The remaining particles (those outside the overlap) are left behind and are no longer tracked or monitored, as their positions remain fixed for the remainder of the simulation.

This simulation is designed to investigate entrainment and detrainment processes by tracking individual candidate particles in both a fixed and a wave-following frame of

reference. Additionally, horizontal Lagrangian transport and particle residence times within the dynamically evolving ISW structure are examined.

Simulation B

The second set of simulations is designed to perform LCS analysis. In this case, no particles are carried over between successive windows. Instead, in each window, a new set of $\approx$ 2.3 million particles is initialized, effectively placing one particle per grid point within the window. Particle trajectories are computed over finite-time integration intervals strictly within each overlapping window, with the maximum interval determined by the corresponding wave propagation through that window. These trajectories are then used to compute forward- and backward-in-time FTLEs, as described in Appendix B.

This simulation is designed to investigate potentially isolated flow topologies, and specifically, the recirculating core, from a Lagrangian perspective. Dynamically important regions characterized by elevated strain and vorticity associated with the ISW core are examined in conjunction with the Eulerian analysis to study entrainment and detrainment processes, as well as to estimate the size of the core.

3 Results

High-amplitude, convectively unstable ISWs shoaling over gentle slopes, such as those found in the SCS (see Fig. 1a and b, respectively), have been recently investigated through both 2D (He et al. 2019; Rivera-Rosario et al. 2020) and three-dimensional (3D) (Rivera-Rosario et al. 2022; Diamantopoulos et al. 2022; Bolioudakis et al. 2025) numerical simulations. The potential for the formation of a subsurface recirculating core (often referred to as a trapped core) and its dependence on background stratification, current, and the associated vorticity field was specifically examined in He et al. (2019), though using an idealized two-slope bathymetry. In contrast, Rivera-Rosario

et al. (2020) employed a realistic bathymetric transect identical to the one measured in situ and used in the present study (see Fig. 1a). Compared to Rivera-Rosario et al. (2020), the present study features improved spatial resolution, by a factor of 2–3 in both directions, enabled by the use of variable-sized spectral elements (as opposed to uniform-sized elements), while also incorporating neutrally buoyant particles.

To provide context for the subsequent analysis, it should be noted that the present two-dimensional simulations do not reproduce shear instabilities (see Appendix B of Bolioudakis et al. (2025)). Within this limitation, four principal stages of ISW evolution are observed and summarized below:

1. The simulated ISW exhibits a marginally unstable condition ($U_{\max} \simeq C$) between approximately 28 and 43 km along the transect (see Fig. 1 and 7). In this first stage, vorticity generated by baroclinic effects (He et al. 2019) is amplified at the rear of the wave. Two weak, counter-rotating vortical structures gradually form within the wave interior. Simultaneously, a thin layer of negative vorticity, already weakly formed in the rear of the wave and extending into its wake, rapidly intensifies at the interface between these structures and penetrates into the wave's interior. This vorticity layer appears to serve as the principal pathway for the detrainment of particles from the core.
2. During shoaling in the second stage, between 43 and 50 km, the marginally unstable conditions of the first stage evolve into what resembles a weak initial convective breaking event ($U_{\max} \geq C$), although $U_{\max}$ still remains close to the propagation speed. At this stage, a distinct vortex dipole is now observed within the ISW, playing a central role in the formation and shape of the subsurface core.
3. In the third stage, between 50 and 63 km, as the wave shoals over the steepest part of the transect and $U_{\max}$ exceeds C, a vigorous main breaking event occurs. Heavier water plunges into the wave interior, and the previous vortex dipole gives way to

smaller, less organized vortical structures. Concurrently, entrainment into the wave core intensifies, with inflow predominantly from the rear shoulder of the wave.

4. The fourth and final stage, between 63 and 74 km, is characterized by a persistently unstable ISW. The core gradually increases in size, and entrainment now occurs not only from the rear, but also from both the top and bottom of the wave core. However, detrainment remains primarily associated with the thin vorticity layer at the wave's tail.

   The dynamical evolution of ISW and its interaction with selected Lagrangian particles across all four stages is illustrated in the animation provided as supplementary material.

The following sections systematically analyze the key dynamical features introduced above. The first stage, and the connection between baroclinically generated vorticity and the formation of the vortex dipole within the wave interior, is examined in Sec. 3.1.1. The formation of the subsurface core is explored in Sec. 3.1.2 using streamlines, vorticity, and density contours, overlaid with particle distributions. Particular attention is given to identifying regions of strong vorticity and strain using Lagrangian metrics, and assessing their potential connection to the entrainment and detrainment pathways of Lagrangian particles. The development and subsequent growth of the core are investigated in Sec. 3.1.3, with comparisons between the traditional $U_{\max}/C$ criterion and the LCS-based analysis. Section 3.2 presents a quantitative comparison of selected particle trajectories and velocities relative to the Eulerian ISW $U_{\max}$ and C metrics. Finally, horizontal particle drift, transport, and residence times within the wave are examined in Sec. 3.3.

3.1 Flow Structure and Particle Distribution During Wave Evolution

3.1.1 Baroclinic Vorticity Generation and Dipole Formation: Eulerian View

Baroclinic vorticity generation under the Boussinesq approximation is defined as $D\omega_y^{\text{baroclinic}}/Dt = (g/\rho_0) \cdot (\partial\rho'/\partial x)$ (He et al. 2019; Sutherland 2010). Initially, a stably propagating DJL-type ISW of depression traveling from left to right over uniform depth generates *oppositely signed baroclinic vorticity* in the rear and front halves of the wave (see Fig. 2a). On the *rear side* of the wave (to the left of the trough), the baroclinically driven component of vorticity is negative *(counter-clockwise)*, since density decreases in the direction of propagation (i.e., from heavier fluid toward lighter fluid depressed by the wave). The *front half* of the wave exhibits the opposite behavior, where density increases with x, resulting in positive *(clockwise)* baroclinic vorticity (see Fig. 2a and He et al. (2019)). The steeper the isopycnal depression induced by the wave, linked to higher-amplitude ISWs and the associated intensification of the pycnocline depression, the sharper the horizontal density gradient $\partial\rho/\partial x$, and thus the larger the baroclinically vorticity generation.

As the ISW shoals toward shallower water, bathymetric effects become increasingly significant within the wave interior. The waveform of the ISW, as indicated by the characteristic displacement of the pycnocline (Fig. 2 between the light and dark gray shaded regions; see the streamline passing through this point), remains remarkably symmetric. However, when focusing on the internal stability of the lighter isopycnals, the *front* of the long wave decelerates slightly relative to the *rear*, due to its earlier interaction with the variable bathymetry. In response, the *rear* of the wave steepens within the ISW interior (while $U_{max} \approx C$), as illustrated in Fig. 2a. This steepening

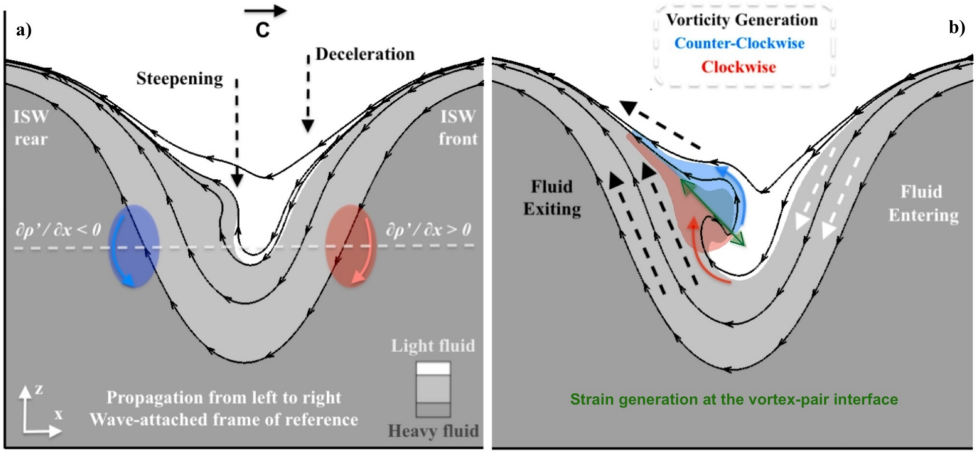

Fig. 2 Cartoon of vortex dipole formation within the ISW. The shading of the density isocontours creates a layered appearance; however, the stratification is continuous. Rear steepening is illustrated by the detaching isopycnal, which would be symmetric to the front in a stably propagating ISW. Blue and red shaded regions indicate negative (clockwise) and positive (counter-clockwise) vorticity, respectively. The colored regions correspond to baroclinically generated vorticity in panel (a), and to total vorticity in panel (b). Green arrow (panel b) highlights the region of strong strain generation.

is primarily manifested in the lighter isopycnals situated above the symmetric waveform, strengthening the local horizontal density gradient and thereby intensifying the generation of negative baroclinic vorticity.

Simultaneously, the near-surface *background vorticity* is also negative. However, closer examination of horizontal velocity profiles at the wake of the wave (not explicitly shown) does not indicate any direct impact of the background current on the formation of vortical structures near the wave interior.

Further upslope, during the transition between marginal ($U_{max} \approx C$) and convective ($U_{max} \geq C$) instability (see also Bolioudakis et al. (2025), Figure 5), the negative baroclinically generated vorticity at the wave rear, in conjunction with the descending heavier fluid driven by the steepening of the detaching isopycnals, leads to the formation of a patch of negative vorticity within the ISW interior. Concurrently, as shown by the streamlines computed in the wave-attached frame of reference, fluid entering the wave from the front is forced into a circular motion, following the depression induced by the wave but not necessarily linked to the baroclinic vorticity component at the

ISW front. This fluid wraps around the wave interior and exits at the rear, inducing a counter-rotating motion just beneath the negative vorticity patch (see Fig. 2b).

The interaction between these two motions described above generates a *vortex pair* as depicted in the cartoon in Fig. 2b; a dipole composed of two counter-rotating vorticity structures (also noted in Lamb (2002)). Furthermore, the calculation of the advective term $(u\partial\omega/\partial x + w\partial\omega/\partial z)$ of the vorticity equation exhibits elongated, banded structures aligned with the flow geometry. Although advection of vorticity between the rear shoulder of the wave and its interior does take place, there is no clear evidence of opposite-sign vorticity patches explicitly imported from the rear and being advected into the wave interior. Hence, the vortex dipole appears to be generated in situ, primarily affected by baroclinic production at the steepening isopycnals and then organized, amplified, and transported by advection. Lastly, at the interface between these vortices, *strong strain* occurs.

3.1.2 Subsurface Core Formation: Eulerian vs Lagrangian view

Figure 3 illustrates the ISW flow structure and associated particles from Simulation *A* (see Sec. 2.4) after the onset of convective instability, at three selected locations along the steepest part of the simulated transect (50-60 km). Streamlines, vorticity, and density contour panels (top, middle and bottom respectively) span 1 km in the horizontal direction ($\approx 1\ \lambda_w$) and are centered on the wave trough. The ISW appears visibly broader at later snapshots captured at increasing upslope positions, consistent with the findings of Rivera-Rosario et al. (2020, 2022); Bolioudakis et al. (2025). For a more detailed and dynamic view of the ISW evolution, the reader is referred to the supplementary animation.

Coherent vortical structures

The top panels (a–c) of Fig. 3 show streamlines computed in a reference frame moving with the wave, overlaid with three isocontours, including two key isopycnals:

$\sigma = 22.58$ kg/m^3 (the pycnocline) and $\sigma = 22.26$ kg/m^3; the latter is highlighted in red in panels (g–i) for reference. The pycnocline serves as a consistent indicator of the symmetric waveform throughout the simulation, while the lighter isopycnal ($\sigma = 22.26$kg/m^3) appears to be the first to illustrate the onset of convective instability under the given background stratification and current.

In panel (a), a pair of fully-formed counter-rotating vortices (see blue-negative and red-positive colored arrow used to indicate vorticity sign) with closed streamlines is observed (indicative of a trapped core Aigner et al. (1999)). This snapshot is taken approximately four wavelengths ahead in the upslope direction, relative to the right panel of Fig. 2. This structure agrees with findings from both 2D and 3D simulations (Rivera-Rosario et al. 2020; Bolioudakis et al. 2025), as well as in situ shipboard measurements (Lien et al. 2012). One of the streamlines passes below the positive (red) vortical structure, curves rearward, then turns forward and enters the vortex pair toward the wave interior, before arcing over the negative (blue) vortex and exiting toward the wave's rear. This streamline exhibits clear signs of stretching and strain, and notably encloses the negative-vortical structure on the rear flank of the wave.

In the region marked by an orange diamond, the velocity vector indicates a trajectory with an inflection point, after which a hyperbolic point (often referred to as a saddle point) is identified (Strogatz 2018; Shadden et al. 2005; D'Ovidio et al. 2009; Aref 1984). This special type of stagnation point (Ide et al. 2002; Shadden et al. 2006) is characterized by fluid converging along one direction and diverging along the other, a flow pattern directly associated with stable and unstable manifolds (Haller 2015). Such structures provide important information about particle pathways and transport barriers.

The identification of hyperbolic points (Strogatz 2018; Haller 2002) follows a two-step procedure. First, grid points with total velocity magnitude ($|U_{total}| = \sqrt{(u + U(z))^2 + w^2}$) approximated as zero are masked; typically, these are points

where $|U_{total}|$ is at least three orders of magnitude smaller than its maximum value within the domain. Second, among these candidates, the Jacobian matrix ($J = \nabla \mathbf{u}$) is evaluated, and points where it has two real eigenvalues of opposite sign are retained.

The streamline evolution in panel (b) suggests that the counter-rotating vortices persist over a focused temporal and spatial window, growing in size as the wave propagates. At this time, two hyperbolic points are identified (also marked with orange diamonds). This configuration closely resembles the schematic presented in Lien et al. (2012) (see their Fig. 2d): a pair of counter-rotating vortices and two stagnation points, as observed in field measurements. By panel (c), additional vortical structures with closed streamlines emerge alongside the two dominant vortices. The interior flow becomes increasingly complex, giving rise to weaker, short-lived vortical structures further upslope. From this stage onward, the hyperbolic points are associated with these secondary vortices and are therefore linked to the flow within the core, rather than to its boundaries and exchange with the exterior.

Vorticity structures, particle layout and primary entrainment/detrainment pathways

In Fig 3, the middle panels (d–f), show vorticity contours (ω_y) along with all particle positions, regardless of location of insertion, within the visualization window. The particle positions align closely with the underlying vortical structures. In panel (d), the counter-rotating vortex pair, observed in panel (a) and discussed via Fig 2b, is also evident, with a geometry qualitatively similar to a symmetric vortex dipole as described in Kramer et al. (2007). This vortex pair appears to play a central role in the early formation of the convectively unstable recirculating core within the wave interior.

As these vortical structures evolve, a distinct thin band of negative vorticity becomes visible at the interface and rear of the dipole (panel e), consistent with observations of shoaling ISWs with surface core formation examined through numerical

simulations in Lamb (2002). This negative vorticity layer acts as a transport pathway, along which particles exchange between the wave interior and its surroundings. Specifically, particles already within the ISW tend to exit along the upper segment of this layer, while particles recirculating outside the wave re-enter the interior along its lower edge. The shape of this layer resembles a tendril that forms as a weak structure at earlier stages of ISW evolution and is gradually amplified. The exact origins of this tendril are outside the scope of this paper. However, both its magnitude and thickness increase notably between 55 and 59 km along the steepest part of the transect (from panel e to f).

In panel (f), this vorticity layer clearly acts as a conduit for material entrainment. Particles located just below the layer are advected forward and enter the wave interior (see the region between 58.8–59 km and depths from 75 to 125 m). Meanwhile, particles positioned above the vorticity layer continue to converge along streamlines that ultimately exit the ISW at its upper trailing edge. For a more complete and dynamic view of this exchange process, the reader is referred to the supplementary animation.

Isopycnals and particle layout

The bottom panels (g–i) of Fig. 3 display the density field, overlaid with all interacting particles shown previously. In panel (g), the red isopycnal ($\sigma = 22.26\,\mathrm{kg/m^3}$) clearly illustrates the deformation of the density structure due to the vortex dipole identified and discussed above. In panel (h), the same isopycnal continues to be shaped by the dominant vortical structures of the wave's convectively unstable core. At this stage, the observed density overturns mark the clear onset of recirculating core formation, as similarly discussed in He et al. (2019).

At the final snapshot (panel i), a vigorous plunge of dense water is observed, resembling the onset of the turbulent gravity current suggested in Bolioudakis et al. (2025). Isopycnals heavier than $\sigma = 22.26\,\mathrm{kg/m^3}$, along with the associated particles, are seen to plunge into the interior of the wave. This stage coincides with the wave

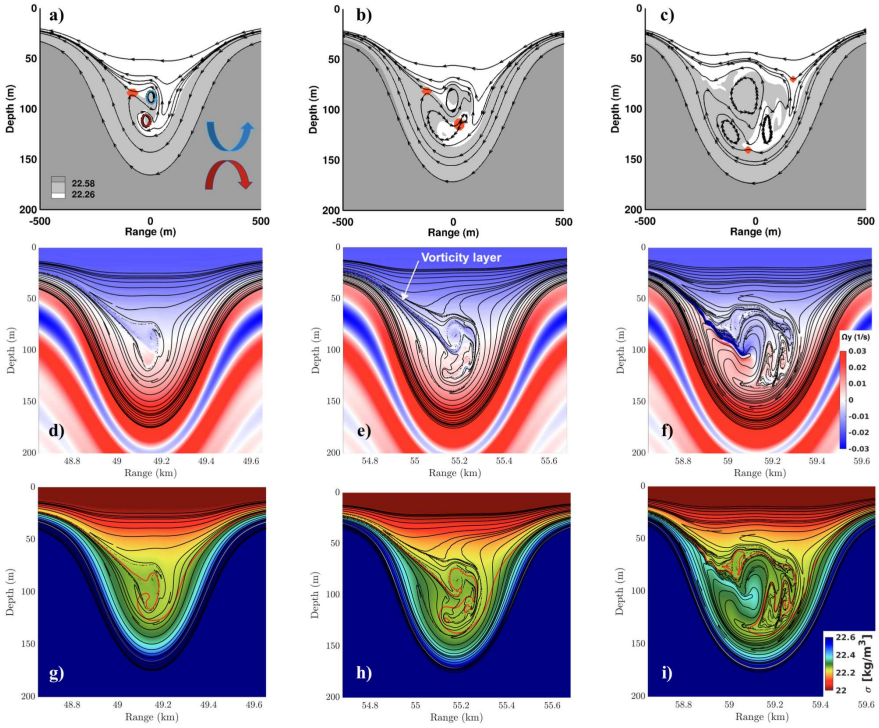

Fig. 3 Snapshots at three locations (ISW trough at 49.15, 55.18, and 59.15 km, from left to right) along the ISW shoaling path after the onset of convective instability, as the ISW approaches and crosses the steepest part of the transect. Top panels: streamlines computed in a wave-attached frame of reference, overlaid on three representative density isocontours, with regions where hyperbolic points are computed, marked by orange diamond symbols. The blue and red arrows in panel *a* indicate the vorticity direction of the closed-streamline structures, counter-clockwise and clockwise, respectively. Middle panels: lateral vorticity ω_y contours with particle positions shown as black-colored particles. Bottom panels: density contours with particle positions also shown as black-colored particles. The red contour line illustrates the $\sigma = 22.26\,\mathrm{kg/m^3}$ isopycnal.

propagating over the steepest section of the transect, where it decelerates and the intensity of the convective instability is amplified (see Sec. 3.2 and Fig. 7).

Isopycnals outside the colorbar range ($[22\ 22.6]\ kg/m^3$) act as persistent particle transport barriers throughout the simulation: particles do not enter the ISW from either the top or bottom beyond these density limits (see Sec. 3.3 and Fig. 9). However, the specific isopycnals through which particles are entrained into the core evolve dynamically during shoaling, with progressively heavier layers becoming convectively unstable and allowing particles to enter the wave interior (see Sec. 3.3).

Lagrangian Coherent Structure Perspective

Ridges of high FTLE values correspond to LCSs, which identify unstable (repelling) and stable (attracting) manifolds revealed by forward and backward-time FTLE fields, respectively. Figure 4 shows the forward- (panels a, c) and backward-time (panels b, d) FTLE fields. The horizontal axis variable, $X/\lambda_w = (x - x_c)/\lambda_w$, denotes the distance from the wave centerline, normalized by the initial ISW wavelength. The FTLE calculations follow the procedure described in Sec. 2.4 and Appendix B, and are computed over a time window of 11 minutes, which corresponds to approximately one wavelength of upslope wave propagation. The choice of time interval is short enough to capture similarities with the Eulerian instantaneous metrics, while also accounting for sufficiently large particle displacements such that potentially isolated flow topologies become visible. The pycnocline is overlaid on all FTLE panels to serve as a reference for the ISW waveform.

In Fig. 4, the regions of highest FTLE values, particularly near the pycnocline and below it, predominantly reflect the large-scale structure of the ISW. Visual inspection suggests that the core is confined within a green-shaded region in the wave interior, appearing well-isolated from the surrounding flow in both the forward and backward FTLE fields. Notably, the FTLE isocontour corresponding to 0.5 (highlighted with a dash-dot black line in all FTLE panels) forms a closed boundary that closely delineates the core region (see also Sec. 3.1.3, Fig. 6). Moreover, the forward and backward FTLE fields appear to approximately reflect each other across the wave centerline for each panel pair (a–b and c–d). In the case of an idealized, inviscid, and steady ISW propagating at constant celerity (i.e., a DJL solution), these fields would be expected to exhibit perfect symmetry (Zhang et al. 2024), as the flow is symmetric about the centerline (Lamb 2002). However, the convectively unstable ISW simulated here exhibits a clear asymmetry, particularly at the rear shoulder, where a red FTLE ridge penetrates the green-shaded region within the wave interior in both forward and

backward fields. While this feature marks the onset of the recirculating core formation process, it is consistent with the asymmetry visible in both the vorticity and density contours of Fig. 3, and with equivalent visualizations of the Eulerian Okubo-Weiss criterion (not explicitly shown).

More specifically, in panel (a), within the region $X/\lambda_w \in [-0.25, 0]$ and depth $\in [50, 80]$, a prominent red FTLE ridge is observed to form on the left shoulder of the ISW, penetrating into the green-shaded region that delineates the wave core. Since the forward FTLE highlights repelling LCSs (regions where initially close particles diverge over time), this ridge indicates an area of strong strain and particle separation. In panel (b), although the high-intensity red region is less prominent, the backward FTLE field reveals a similarly elevated FTLE layer extending into the wave interior, forming a tongue-like structure that appears to coincide with the negative vorticity tendril shown in Fig. 3c. This feature indicates an attracting Lagrangian pathway along which particles converge, irrespective of their direction relative to the wave core. This observation aligns with the earlier depiction of the vortex pair and associated negative vorticity layer in Fig. 3, which facilitates both particle entrainment into and detrainment from the wave core.

A similar but more pronounced structure is visible in panels (c) and (d). In panel (c), the forward FTLE field shows a more robust (in color and spatial extent) high-strain region (implying again strong Lagrangian divergence), whose position with respect to the wave is approximated where the top-left saddle point was identified in Fig. 3 (panels a and b). In panel (d), the backward FTLE ridge penetrates deeper into the core than its high strain forward FTLE counterpart, reaching the coherent vortical structure associated with the negative-vorticity lobe of the dipole. This pathway of mutual entrainment and detrainment aligns with the negative-vorticity tendril shown in Fig. 3 (panels d and e), which increases in amplitude and width near the steepest

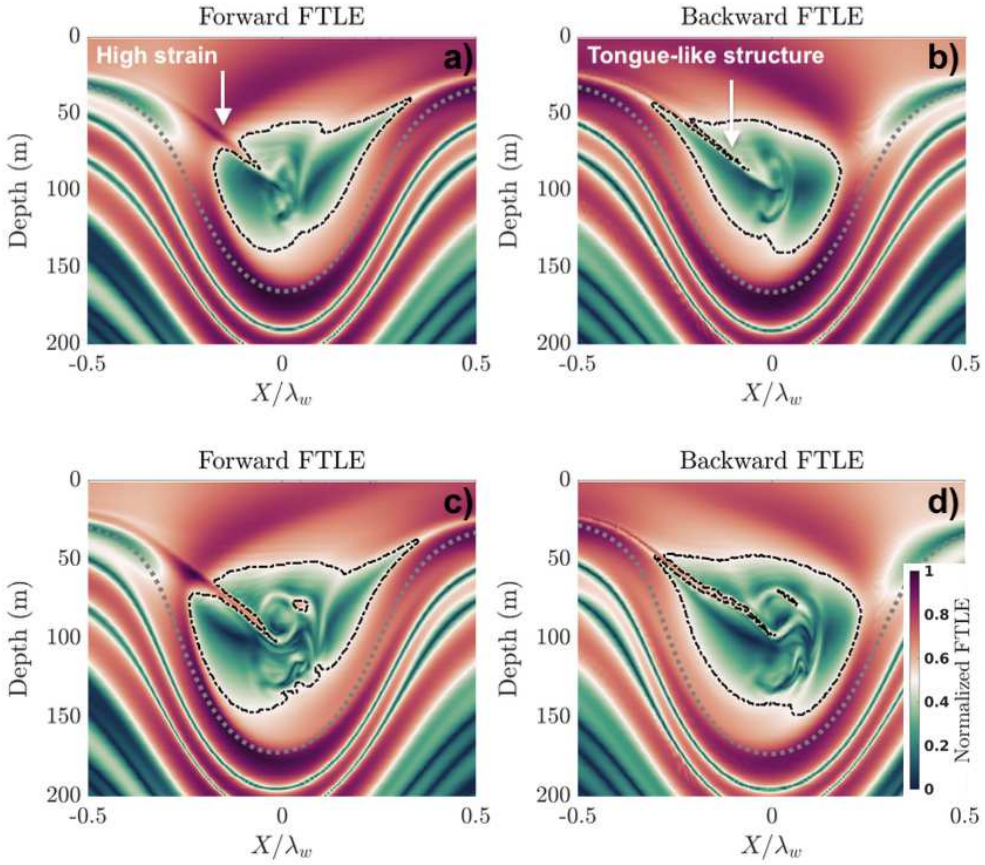

Fig. 4 Forward- and backward-in-time Finite-Time Lyapunov Exponents (FTLE), shown in left and right columns respectively. The black dash-dot line in all panels corresponds to the 0.5 isocontour, which was found to enclose a closed region that visually delineates the isolated green patch associated with the ISW core (see core delineation discussion in Sec. 3.1.3). The x-axis is presented in a wave-attached reference frame ($X = x - x_{\text{trough}}$), and normalized by the initial ISW wavelength ($\lambda_w \approx$ 1 km). The FTLE is computed over a time window of approximately 11 minutes and is normalized by its maximum absolute value. Two snapshots are shown: top and bottom rows correspond to instants separated by approximately six wavelengths. These locations are approximately 1.5 wavelength ahead in the upslope direction from those shown in the left and middle columns of Fig. 3, respectively (50.5 and 56.7 km), corresponding to the region where the counter-rotating vortex dipole dominates the wave interior. The pycnocline is included with a dotted grey line, for reference.

slope segment of the transect. This interpretation is further supported by the particle behavior shown in the supplementary animation.

3.1.3 Subsurface Core Evolution

Figure 5 illustrates the evolution of the simulated ISW as it shoals toward the shallower part of the transect, shown through density contours overlaid with the corresponding particle distribution (obtained from Simulation A). Panel (a) focuses on a 20-km section of the domain, corresponding to the region where the vortex pair forms within the ISW and until near the end of the computational domain upslope. Particles are plotted as dots in two colors: (i) white-colored particles represent particles whose initial position along the transect was < 52 km (the starting point of this panel's frame), while (ii) black-colored particles denote particles injected between 52 and 72 km along the transect. It is important to note that a particle's initial position refers to its *injection location* near the pycnocline, not the time or location at which it may enter the core. This distinction is essential to emphasize that particles require time to interact with the wave and, at least in the early stages of entrainment, descend from the front toward the rear while circulating around the waveform, before becoming entrained through the high-strain/vorticity region discussed in Sec. 3.1.2. Panel (b) corresponds to the final stage of the vigorous plunge discussed earlier and shown in the right column of Fig. 3. Panels (c) and (d) follow the wave as it shoals toward the shallower, nearly uniform-depth plateau of the simulated transect.

Particle interaction with the evolving ISW

White-colored particles in Fig. 5a were injected earlier along the transect and subsequently advected with the ISW, thereby illustrating upslope horizontal particle transport. At the time of this snapshot, these entrained white particles are found either within the wave core or wake. Those that remain within the core are distributed primarily across its upper region. Those located near the rear shoulder and in the wake of the ISW are concentrated along a narrow band that coincides with the detrainment pathway facilitated by the negative-vorticity layer (or tendril) discussed in Sec. 3.1.2.

This observation suggests that detrainment occurs mainly through a confined path at the trailing edge of the ISW, with its width dynamically governed by the thickness of the underlying vorticity tendril.

Examining the zoomed-in panels (b–d), white-colored particles are predominantly located at the front and upper portions of the ISW core (panel b). As the wave propagates and broadens, the core expands, accommodating more particles into its interior (panels c and d). These white particles, though, remain largely confined to the upper core and follow a broad circulation from front to rear, ultimately positioning near the upper part of the tendril.

Supplementary animations suggest that, along the largest segment of the transect, detrainment primarily occurs along the upper part of the vorticity tendril, while its lower edge is linked to rear-entrainment features. Consequently, the white particles, associated with earlier-phase entrainment (Fig. 3g,h), are more likely to exit along this upper detrainment pathway than the black particles. Finally, in panel (c), a large negative-vorticity vortex forms near Range $\approx$ 65.1 km and depth $\approx$ 60 m, evolving into a coherent material structure (see magenta annotation) that exits the wave rearward (panel d, Range $\approx$ 70 km, depth $\approx$ 40 m), carrying a cluster of particles and thereby locally enhancing detrainment.

Black-colored particles in Fig. 5 are also found both within the ISW core and in its wake. In panel (b), coherent lines of black particles are observed bending from the rear of the wave and being advected toward the wave interior as part of the vigorous isopycnal plunge. In panel (c), the lower portion of the core is largely occupied by black particles, now appearing in a more diffuse and dispersed distribution compared to the coherent alignment seen in panel (b), governed by the descending fluid and the associated plunge. In panel (d), the black-colored particle population dominates the bottom of the core, extending from the rear to the front. However, stirring induced by the vortical structures in the wave interior has redistributed the particles, resulting

in a more diffuse and mixed pattern. White- and black-colored particles now appear interspersed throughout the core, with individual particles of each color present across most regions.

From the perspective of entrainment, and particularly between panels (c) and (d), particles are no longer forced to enter the core exclusively through the rear shoulder and the associated negative-vorticity layer, as was the case during the core formation stage. Instead, as shown in panels (c) and (d), black particles are also entrained through smaller, transient pathways located near the bottom-front and top portions of the core. These regions appear as disruptions, or "cracks", in the otherwise uniform particle distribution and are associated with short-lived vortical structures propagating through the wave interior (see also supplementary animation). This observation is corroborated by additional red ridges in the visualization of the FTLE fields in later times (equivalent to those of Fig. 4 - not explicitly shown here), which penetrate the ISW core from the top and bottom at these later stages of wave evolution. Therefore, entrainment initially occurs predominantly at the wave rear, with most particles captured during the convective plunge (Fig. 3, right column; Fig. 5b). However, as the wave propagates into shallower regions, the process evolves, and simultaneous entrainment pathways emerge from both the top and bottom of the core.

Core delineation metrics

The size of the recirculating core increases visibly as the convective instability intensifies and the ISW entrains more particles while shoaling over shallower waters. This growth is evident from the broadening of the waveform and the evolving particle distribution shown in Fig. 5, panels b), c), and d). In the literature, including numerical, laboratory, and observational studies (Lamb 2002; Lien et al. 2012; He et al. 2019; Zhang and Alford 2015; Carr and Davies 2008), the extent of the convectively unstable region and the associated recirculating core is typically estimated using closed streamlines in a wave-attached reference frame or by identifying regions where the

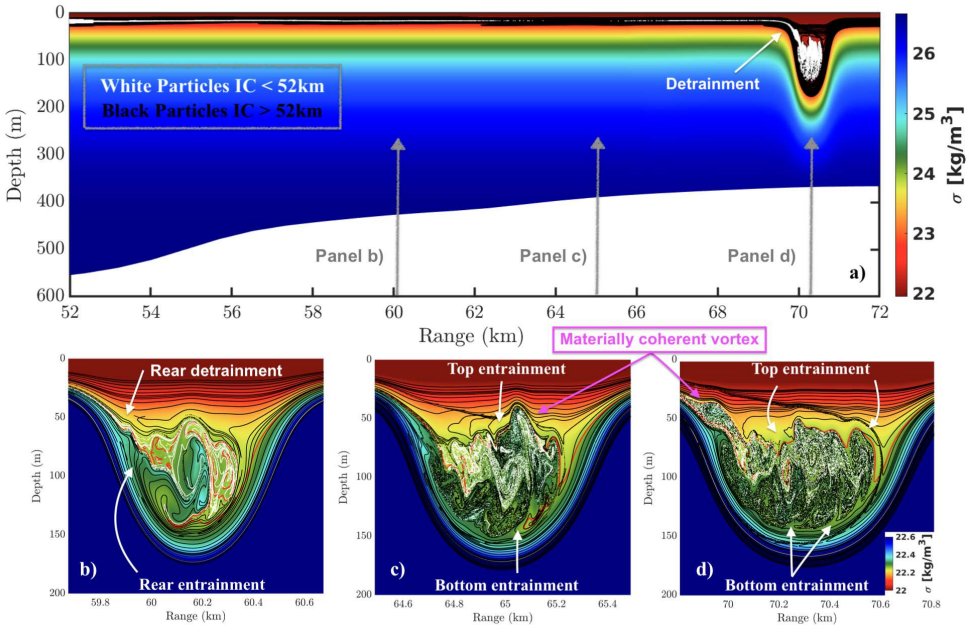

Fig. 5 Density contours showing the propagation of the ISW toward the end of the computational domain. The top panel provides a wide field of view spanning 20 km, capturing the ISW's evolution as it traverses the steepest segment of the transect and approaches the nearly uniform plateau. White and black colored particles denote particles that were initially seeded before <52 km and between 52 and 72 km of the transect, respectively. The bottom panels present a zoomed view of the ISW's evolving structure, highlighting entrainment/detrainment pathways between the core and its environment. The magenta annotation emphasizes a materially coherent vortical structure transporting a cluster of particles. Gray vertical arrows in the top panel indicate the instantaneous positions of the ISW trough. Note that the colorbar limits differ between the top and bottom panels; the zoomed views employ a narrower range to better emphasize the internal structure of the wave core.

wave-induced horizontal velocity approximately matches the wave celerity ($U_{\max} \simeq C$). In contrast, Luzzatto-Fegiz and Helfrich (2014) proposed a Lagrangian approach, defining the core as the region enclosed by intersecting forward and backward FTLE ridges, providing a more robust and physically meaningful delineation.

Searching for closed streamlines to delineate the core proves ineffective, as the wave interior, following the formation of the subsurface core and the establishment of the counter-rotating vortex pair, is populated by numerous smaller and short-lived vortical structures (e.g., Fig. 3c). Consequently, no single closed streamline reliably characterizes the core region.

To assess the core boundaries and its evolution, we compare the Eulerian $U_{\max} = C$ criterion with the LCS-based boundary of Luzzatto-Fegiz and Helfrich (2014) at four representative locations along the transect. In Fig. 6, the $U_{\max} = C$ contour, evaluated instantaneously, is plotted as a magenta dashed line. The LCS computation is based on Simulation B (see Sec. 2.4) and is performed once per window (W6-W9). The FTLE fields used to identify LCSs are calculated over a longer time window corresponding to approximately $5\,\lambda_w$ of upslope propagation, in contrast to that $1\,\lambda_w$ integration used in Fig. 4. This extended time window improves the capture of cumulative flow map deformation ($D\Phi$; see Appendix B), providing a more accurate delineation of regions containing long-residence particles. Following Luzzatto-Fegiz and Helfrich (2014), LCSs are defined by the intersection of forward- and backward-time FTLE ridges that form closed boundaries. In our simulation, the selected intersecting ridges correspond to a normalized absolute FTLE value of 0.5 (see Fig. 4). The black scattered points in all panels of Fig. 6 mark the outer boundary of these intersecting ridges and effectively define the LCS. The green-shaded region enclosed by this boundary denotes the ISW core area. Lastly, the pycnocline is plotted (gray dotted line), and the centerline position is indicated (bottom-left corner of each panel), as the horizontal-axis uses the normalized coordinate X/λ_w to provide a clearer representation of the core size.

The Eulerian $U_{\max} = C$ magenta contour shows close agreement with the LCS-based prediction of the recirculating core. As the ISW shoals into shallower waters, the estimated core size increases (clearly reflected by both methods) in agreement with the broadening of the waveform and the greater number of entrained particles. The LCS-based core (green contoured area) appears more clearly defined and symmetric about the centerline, likely reflecting the influence of long-term particle residence, in contrast to the instantaneous and transient nature of the $U_{\max} = C$ criterion. Although temporally averaged $U_{\max} = C$ contours were also computed (not explicitly shown), the results did not yield significantly different conclusions.

The horizontal extent of the core shows strong agreement across all panels between the two approaches. However, the most notable differences lie in the estimated vertical extent, particularly between windows W8 and W9. In all cases, the LCS-based estimate extends further vertically, both upward and downward, than the Eulerian prediction. This discrepancy may be attributed to regions that lie outside the magenta contour but inside the LCS boundary, where local velocities fall just below the wave celerity. Such regions could correspond to fluid parcels circulating rearward within the core, while still being carried forward with the ISW. In this scenario, the local horizontal velocity would be negative in the wave-attached frame, thus not satisfying the $U_{\max} = C$ criterion, even though the particles remain materially trapped over time. Alternatively, these regions may represent zones of transient entrapment, where particles are temporarily transported with the wave but are not ultimately entrained.

Lastly, a third method was employed to examine the core boundaries: for particles that remained entrained and traveled at least 10 km with the ISW, the outermost trajectories in the wave-attached frame were analyzed (not explicitly shown). The recirculating core, as delineated by this method, is well-approximated by an ellipsoidal shape whose major (x) and minor (z) axes expand as the wave shoals upslope. For the four snapshots shown in Fig. 6, the core regions estimated by all three methods are roughly centered around the same location and overlap substantially. Among them, the $U_{\max} = C$ estimate yields the smallest area, the LCS-based estimate is larger, and the ellipsoidal envelope is the most expansive, especially in the vertical direction. Across windows W6 to W9 (panels a to d), the surface area enclosed by the LCS-based core increases from approximately 8,500 m^2 to 34,000 m^2, with all three approaches yielding estimates on the order of 10^4 m^2.

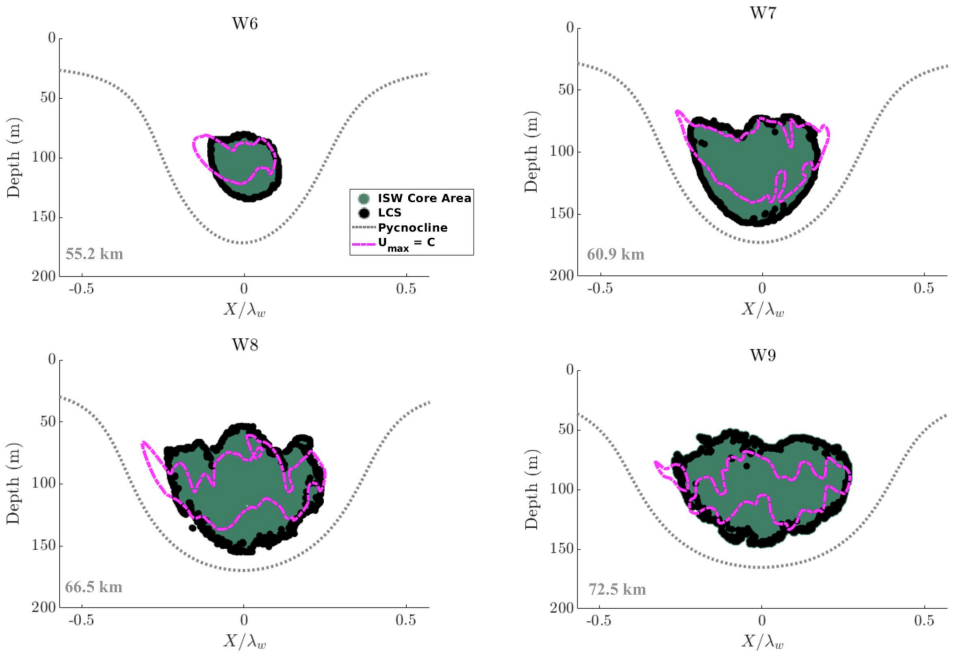

Fig. 6 Evolution of the core boundaries and associated area as depicted by Lagrangian Coherent Structures computed over a time window of approximately 1 hour (black outline and green-shaded region), compared to the Eulerian $U_{\max} = C$ metric evaluated at a single time step (magenta dashed line). Four snapshots are shown, corresponding to the final 4 overlapping windows of the simulation. The location of the ISW trough with respect to the transect is indicated in the bottom-left corner of each panel. The pycnocline is plotted as a gray dotted line, for reference.

3.2 Lagrangian Particle Velocity and Motion

Figure 7 presents the velocity of selected particles (U_p; black solid lines) relative to the ISW propagation speed, shown in panel (a), as a function of along-shoaling-track wave-center position. The plotted particles (≈ 1500) are chosen among others based on their long-distance transport with the wave, having remained entrained and traveled approximately 30 km upslope. In the reference frame moving with the wave ($C = 0$), the dashed blue line serves as a reference; points above and below this line indicate faster and slower motion with respect to wave propagation, respectively. Additionally, the Eulerian maximum wave-induced velocity in the same frame ($U_{\max} - C$) is shown with a red solid line.

The evolution of $U_{\max}$ and C follows a similar trend to the equivalent three-dimensional simulation presented in Bolioudakis et al. (2025). In deeper waters (not shown here), the ISW propagates in a stable manner. Between approximately 28 km and 43 km along the transect, dashed blue and solid red curves largely overlap, as the wave undergoes an initial weak convectively unstable event, and effectively enters a marginally unstable regime where $U_{\max} \simeq C$. Beyond 43 km, the condition $U_{\max} > C$ is consistently satisfied, indicating the onset of convective-instability-dominated regime. As the wave encounters the steepest portion of the slope (53-58 km), it decelerates significantly, while U_{max} remains non-trivially higher, thereby amplifying the convective instability and initiating a vigorous gravity-current-like plunge within the wave interior (around 59 km; see Fig. 3i). This convectively unstable regime persists until the end of the simulation, with both U_{max} and C gradually decreasing as the wave shoals over shallower waters.

From a Lagrangian perspective, the particles are initially positioned near the pycnocline region (see Sec. 2.4, Simulation A). Their initial velocity is negative, consistent with the background current (see Fig. 1b) at each particle's vertical position. In the wave-attached frame of reference considered here, the initial particle velocity is given by $U_p^{\text{init}} = U(z) - C$. As the ISW approaches, the particles experience a notable reduction in velocity magnitude, between approximately 38-43 km along the transect. This absolute velocity deceleration corresponds to the particles interacting with the wave and gradually slowing down as they become entrained, accompanied by a vertical acceleration (not shown). In contrast, at an inertial (fixed) frame of reference, this transition would manifest as a significant acceleration, as the particle velocity shifts from its initial background value $U_{p-fixed}^{\text{init}} = U(z)$ to a velocity matching the wave celerity, i.e., $U_{p-fixed} \approx C$.

During the entrainment phase (approximately 38-50 km), most of the black curves remain below or close to the wave celerity. This occurs because the particles must

circulate around the core from below, moving in the negative relative direction with respect to the wave, before entering the core through the pathway defined by the vortex dipole and the associated negative-vorticity layer shown in Fig. 3. Following the entrainment of the selected particles (Fig. 7 Range $>$ 50 km and $U_p - C > 0$), the particle velocity U_p exhibits an oscillatory pattern relative to C. To highlight this behavior, panel (b) of Fig. 7 presents a zoomed-in view (not to scale) between 60-70 km, where two, randomly selected, example particles are plotted with dotted and dashed black lines, respectively, and compared against C (blue dashed line). The observed oscillations are caused by the particles' relative motion inside the wave core: as they circulate toward the rear, they appear to decelerate (moving against the wave direction), and as they move toward the front, their velocity exceeds C. Importantly, there is no single characteristic recirculation period, as the flow within the core is dynamically evolving and influenced by smaller-scale vortical structures.

During the 60-70 km segment, the histogram of particle velocities shown in Fig. 7 ($U_p - C$; histogram not explicitly shown) approximates a Gaussian distribution, slightly skewed toward negative values, with a median of -0.0053 m/s and a standard deviation of 0.0734 m/s. From Fig. 7, upper and lower bounds for $U_p - C$ can be estimated for particles that remain trapped and recirculate within the core. The upper bound is constrained by the flow's maximum velocity, $U_{\max}$; in our case, the highest value observed among particles is 0.23 m/s (corresponding to approximately 1.7 m/s in the fixed frame). The lower bound, determined graphically, lies around -0.35 m/s (approximately 1 m/s in the fixed frame), and will be used in Sec. 3.3.2 to guide the associated residence time analysis. This supports the hypothesis discussed in Sec. 3.1.3 that particles with velocities outside the instantaneous $U_{\max} = C$ topological bound can still remain trapped and be part of the materially coherent core. Therefore, the discrepancy between the LCS-based and $U_{\max} = C$ core boundaries observed in Fig. 6 is well justified.

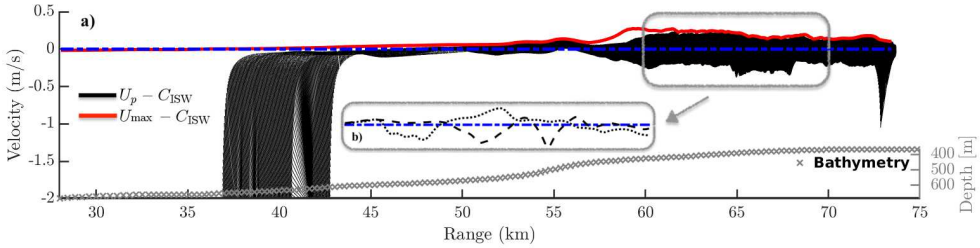

Fig. 7 Velocity comparison in a frame of reference moving with the ISW. In this frame, the ISW's propagation speed is effectively zero and is shown with the dashed blue line in both panels (a) and (b). The maximum ISW-induced horizontal velocity is illustrated with the red solid line. Panel (a) also displays the Lagrangian velocities of selected particles (black lines) that became entrained and traveled long distances with the ISW. Gray "x" markers indicate the bathymetry for reference. Panel (b) presents a zoomed-in view between 60 and 70 km along the transect, highlighting the oscillatory behavior of two example particles around the ISW celerity C.

Finally, a small subset of particles becomes detrained near the 73^{th} km, as indicated by their increasing magnitude of negative velocities. These particles have exited the wave and are no longer carried along with it.

3.2.1 Particle Trajectories

Trajectories of particles transported upslope by the ISW are illustrated in Fig. 8. Two representative particles are shown in both a fixed (left panel) and a wave-attached (right panel) frame of reference, highlighted using *dotted* and *solid* black lines and will be referred to as the *dotted* and *solid* particle, respectively. They originate from the white and black particle groups shown in Fig. 5, with their initial positions marked by circles and final positions by squares (colored blue and cyan, respectively). To maintain visual clarity, only these two representative trajectories are shown.

In the left panel of Fig. 8, the particle pathlines are superimposed on density contours, capturing the ISW evolution up to the end of the simulation. In this fixed frame of reference, the shoreward transport for each particle at hand is clearly visible, with the total horizontal displacement being approximately 24 km for the *dotted* particle and 20 km for the *solid* particle. Both particles initially propagate slightly downslope ($\Delta x \approx -0.65$ km) following their injection, as they are influenced solely by the stable background current prior to interacting with the ISW. Their initial depths are both

above the pycnocline, at approximately 21 m (*dotted*) and 18 m (*solid*), where the local background velocity is $U(z) \simeq -0.5\ m/s$. As the wave approaches, their motion diverges: the *dotted* particle shows a gradual descent as it circulates within the wave core, reaching a maximum depth of approximately 144 m after about 5 km of shoreward travel from its first interaction with the ISW. From that point onward, its motion appears relatively smooth and coherent, with weak vertical oscillations, until its eventual detrainment. In contrast, the *solid* particle undergoes a much quicker entrainment, reaching a depth of roughly 160 m within less than 1 km of horizontal propagation, reflecting a more rapid engagement with the wave. Its trajectory displays pronounced vertical oscillations, indicating frequent changes in vertical velocity and interactions with smaller-scale vortical structures that dominate the interior of the ISW.

This contrast becomes even more apparent in the right panel of Fig. 8, which presents the same trajectories in a wave-attached frame of reference, highlighting the recirculating nature of the ISW core. In both cases, particles that become entrained originate from depths shallower than the pycnocline ahead of the wave (marked as "Entrainment Origin"), shown as a gray dashed line representing the approximate waveform shape. The *dotted* particle follows a tighter recirculating loop before reversing direction and being entrained from the rear of the evolving core, while the *solid* particle follows a broader loop, diving into deeper water before being entrained from the wave's rear shoulder.

Once entrained, both particles interact with the embedded vortical structures. The *dotted* particle follows a relatively smooth path with larger-scale circulation, progressing toward the front of the wave and eventually circling back to the rear before being detrained from the top left shoulder. In contrast, the *solid* particle exhibits a far more complex path with frequent changes in direction, suggesting multiple interactions with finer-scale vortices. Although both particles traverse similar regions within the wave core at overlapping simulation times, their trajectories diverge due to differences in

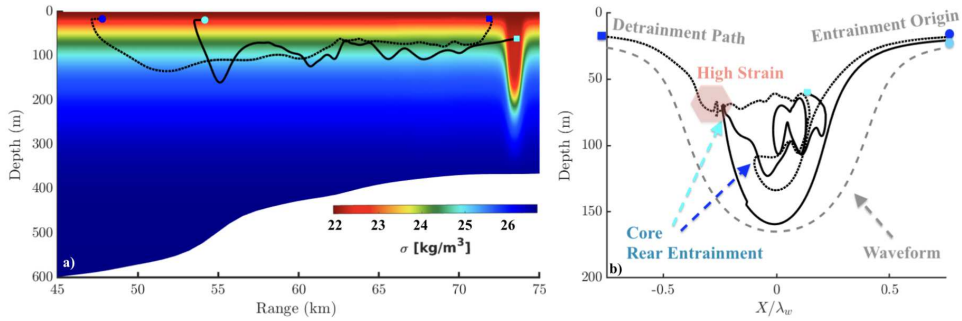

Fig. 8 Particle trajectories for two representative particles shown in both a fixed (left panel) and a moving (right panel) frame of reference. Right panel is focused within the wave. Circles denote their initial positions, while squares mark their final positions. The associated paths that particles follow before interacting with the core and becoming entrained, as well as the paths they follow to leave the wave, are marked.

momentum and local flow dynamics. Notably, the region where the *solid* particle is initially entrained is later revisited by the *dotted* particle just prior to its detrainment. This area, shaded in pale red in Fig. 8b, corresponds to a localized high-strain zone identified in Figs. 3 and 4, and appears capable of supporting both entrainment and detrainment depending on the particle's precise position relative to the vorticity tendril and the associated evolving wave dynamics.

In contrast to the more distributed nature of entrainment, detrainment trajectories tend to appear narrower and more constrained. Focusing again on the *dotted* particle, which is detrained by the end of the simulation, its final depth of approximately 15 m reflects a vertical displacement from its initial position of injection. This suggests that particles stirred within the wave core do not necessarily exit along the same isopycnal on which they were initially seeded. Aside from isolated events such as the materially coherent vortex transported out of the core that locally enhance the detrainment vertical boundaries (see Fig. 5, panels c and d), detrainment is primarily confined to a narrow leaky channel at the rear of the wave (see also Sec. 3.3.1, Fig. 9), corroborating Lamb (2002).

3.3 Particle Transport

Shoreward particulate transport is critically important for coastal processes (see Sec. 1). An idealized, stably propagating ISW without any background current would exhibit a velocity structure that is positive (in the direction of propagation) in its upper portion and negative in its lower portion, thereby symmetrically dispersing the particles it encounters along its path (Garwood et al. 2020). Stastna et al. (2011) discussed the dispersion and transport of stochastically perturbed particles under the influence of a propagating ISW in uniform depth. In contrast to stably propagating ISWs, waves that possess convectively unstable trapped cores are capable of entraining particulate matter and transporting it over long distances, as shown in numerical simulations in uniform depth with and without the influence of a background current (Lamb 1997; Gil 2017), as well as during shoaling (Lamb 2002). In the following part of this section, we analyze a selected particle cloud, representing a subset of the injected particle population located within the core of the simulated high-amplitude ISW at the last snapshot of the simulation, and trace its origin (Sec. 3.3.1). Subsequently, in Sec. 3.3.2, we quantify the net drift and compute the residence times of entrained particles. The results refer to Simulation A (see Sec. 2.4) and account for the shoaling and dynamically evolving ISW under consideration.

3.3.1 Entrainment zone and shoreward travel

Figure 9a shows the particle distribution in the ISW interior, captured at the last snapshot of the simulation. The colored particles visualized within the ISW core represent particles that have been entrained and have traveled with the wave. Each of the six colors corresponds to the distinct, 5 km-long regions along the transect where each of the particular color-coded particles was initially seeded (see the corresponding legend values). Note that the selected particles shown here were initially seeded during windows W3 to W8. Since this snapshot corresponds to the final window (W9), all

displayed particles have been fully entrained and transported by the ISW, not merely influenced by it. Particles seeded in W9 are not included in the plot, as it is non-trivial to determine a priori which of them will become entrained; including them would also compromise visual clarity. Lastly, from the initial cloud of 3306 particles seeded inside the ISW at 28 km, only 10 remained inside the core until the last snapshot. However, as this number is not statistically significant, these 10 particles have also been omitted from the figure.

The gray dotted line in panel (a) corresponds to the $\sigma = 22.4\ kg/m^3$ isopycnal and is used here as a reference for the symmetric waveform. Unlike previous figures, which used the pycnocline ($\sigma = 22.58\ kg/m^3$) as the reference, this slightly lighter isopycnal is selected to better delineate the approximate lower boundary of the leaky detrainment channel. A materially coherent vortex structure, as shown in Fig. 5, can detrain a large number of particles while propagating from the front to the rear of the ISW (see supplementary animation for additional examples). In the absence of such a structure, the detrainment channel is thin, located at the upper rear shoulder of the trailing edge, and largely confined to density values lower than 22.4 kg/m^3. This suggests that, regardless of the isopycnal level at which particles are initially seeded ahead of the wave within the stratified ocean, once entrained, they are ultimately detrained above this density threshold in the ISW wake.

From their distribution, it is evident that particles from all initial injection regions become thoroughly stirred within the ISW core, with individual particles from each group found throughout the core's extent. However, the majority of particles that had been entrained early along the transect (dark red and cyan), primarily through the vortex dipole interface and the associated vorticity layer, tend to accumulate along the top-rear portion of the wave core. In contrast, the green and yellow particles, entrained primarily near the steepest slope and the associated vigorous gravity-current-like plunge, are more broadly dispersed across the bottom half and the front of the

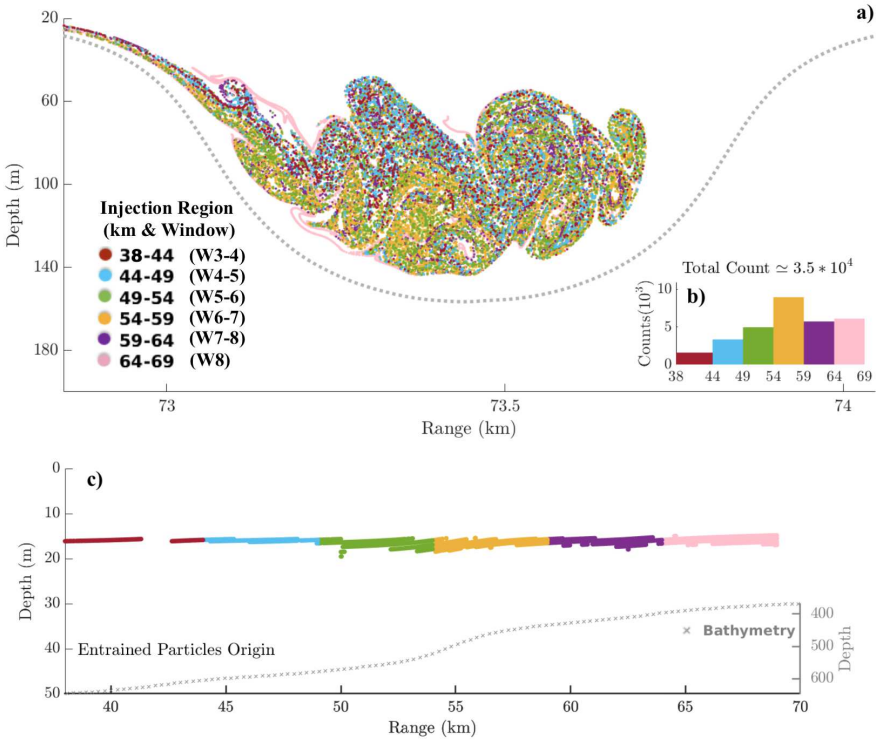

Fig. 9 Panel (a): Particle distribution within the ISW core at the final snapshot of the simulation. All particles shown were carried into this region by the ISW from earlier overlapping windows, ensuring past entrainment. Colors indicate different initial injection regions along the transect. Each corresponding segment is labeled in the legend in kilometers, along with the identifiers of the overlapping windows. The grey dotted line represents the $\sigma = 22.4$ kg/m^3 isopycnal denoting the symmetric waveform. Panel (b): Histogram of particle count per injection region. Panel (c): Initial particle locations along the transect, with bathymetry included for reference. Note the difference in the vertical scales between the left and right vertical axes.

recirculating core. Lastly, particles entrained during the ISW's propagation over the shallower and less steep sections of the transect (purple and pink) are more coherently concentrated near the top and bottom "cracks" of additional entrainment to the core.

The total number of particles found within the ISW at the final simulation snapshot, along with the breakdown by initial seeding region (color), is shown in the histogram in Fig. 9b. This provides a quantitative reference for population differences among the particle groups. The largest count corresponds to the yellow particles, seeded near the steepest part of the transect. Notably, the dark red particles,

though fewer overall, still represent a substantial count, particularly considering they have traveled over $30\,\lambda_w$ with the ISW. This highlights the potential for significant long-range particulate transport by the wave.

Finally, panel (c) of the same figure illustrates the vertical extent of the initial particle injection positions, indicating the vertical variation of the entrainment zone during the ISW propagation. It is evident that all particles ultimately found within the ISW core originate from a confined region located above the pycnocline. The effective entrainment zone, defined here as the vertical extent of the initial seeding region from which particles become entrained, spans depths of approximately 14 to 20 m. This zone is initially even narrower and appears to expand in two key regions: (a) near the steepest slope, and (b) over shallower waters, where entrainment additionally occurs from localized top and bottom regions of the core. This entrainment zone exhibits a relative thickening by a factor of ~ 2 compared to the narrower band observed near 40 km along the transect. Interestingly, there exists a small segment around 43 km where no particles seeded there are found inside the core. This anomaly may be attributed either to the complex internal dynamics of the ISW at that location, where the vortex dipole and the associated vorticity layer are still forming, or to a slight discontinuity in the initial particle positions resulting from the overlap between successive computational windows.

3.3.2 Lagrangian Drift and Residence Time Analysis

In this study, the simulation setup includes a stable background current that, when focusing on the top 250 m of the water column, induces a horizontal velocity always opposite in sign to the direction of wave propagation toward shallower waters ($-0.5 \leq U(z) \leq 0$, see Fig. 1b). Consequently, in the absence of ISWs and given the vertical extent of the injected particles from simulation A, no shoreward particulate transport would be expected.

The maximum offshore displacement a particle could experience within a single computational window due solely to the background current is estimated at approximately 2 km. The final horizontal particle transport results from both background advection and the influence of the shoaling ISW. In the remainder of this study, cases exhibiting relatively small horizontal dispersion (on the order of λ_w), indicative of brief interaction with the ISW without entrainment effects, are not examined in detail.

Instead, focusing on the subset of particles initially seeded during windows W3 to W8, we investigate those whose final horizontal position lies at least 3 km upslope from their initial seeding location. This selection provides a clearer picture of the larger-scale horizontal transport enabled by the ISW dynamics.

Lastly, note that the results are constrained by the finite length of the full-domain simulated bathymetric transect. Therefore, any extrapolation to larger distances upslope should be interpreted with caution, as it may affect the statistical significance of the observed trends.

All 691,550 particles within the pycnocline region from Simulation A were considered, of which 93,354 exhibited shoreward drift exceeding 3 km. Figure 10a shows the distribution of horizontal particle displacement (Δx) as a combined histogram (gray bars; left axis) and cumulative distribution function (CDF; blue curve; right axis). Most particles experienced modest shoreward drift, with a pronounced peak around 3–4 km and a sharp drop-off beyond 8 km. These particles were influenced by the shoaling ISW; they decelerated in a wave-attached frame while circulating the core. However, they were not entrained and ultimately exited into the wave's wake.

A small subset of particles, especially those seeded near the end of window W8, may have continued traveling with the wave beyond the simulation's time span. This limitation must be taken into account when interpreting the results. Meanwhile, the histogram reveals a non-negligible tail extending up to 35 km, indicating substantial transport for a smaller fraction of particles. The CDF rises steeply within the first

10 km, where 70% of particles are transported, and then gradually levels off. This distribution highlights the coexistence of coherent bulk transport of at least 10 km, and the presence of potentially less frequent, high-drift events associated with particles trapped in the subsurface core.

Figure 10b illustrates the same set of particles, now categorized by their initial positions along the transect. The average horizontal distance traveled by particles initially seeded in each corresponding location is shown. The vertical axis is focused on a zoomed-in depth range, corresponding to the subset's entrainment zone previously identified in Fig. 9c. Prior to the 50 km mark, only a narrow vertical band (approximately between 15.5 and 17 m) is associated with long-range transport, highlighting particles that were successfully entrained and remained within the ISW for more than $30\lambda_w$. Between 50 and 60 km, where the ISW shoals over the steepest slope and vigorous plunging occurs within the wave interior, the vertical extent of the entrainment band for long-transporting particles broadens considerably, at least doubling in thickness, consistent with Fig. 9c. This region reflects entrainment from a wider range of isopycnals. In the final 10 km shown in the panel, although the vertical extent of significant transport remains narrower, the average horizontal displacement reaches around 10 km, suggesting a possible underestimation of transport due to the simulation ending near the 74^{th} km of the transect.

Panels (c) and (d) of Fig. 10 present a detailed analysis of particle residence times within the ISW. Again, the analysis begins by filtering Simulation A particles to retain only those that experienced ≥ 3 km of shoreward drift. This subset of particles needs to be further filtered to retain particles that have been entrained by the ISW. Ideally, entrainment could be determined by tracking whether these particles resided within the ISW core; however, due to the core's transient and unsteady nature, and the lack of sharply defined boundaries, such an approach is not feasible. Instead, a velocity-based criterion is employed to robustly determine entrainment: a particle is

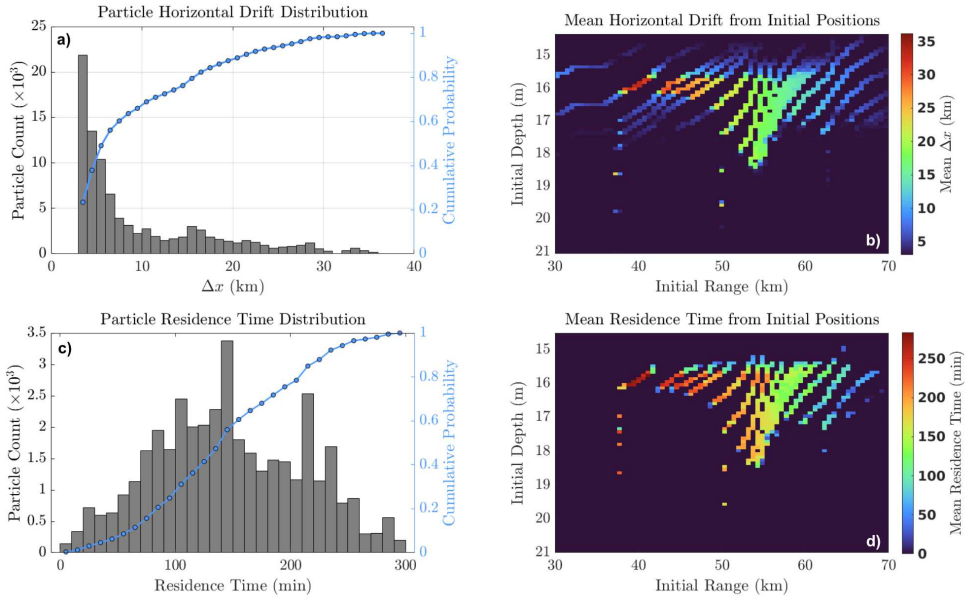

Fig. 10 A combined CDF and histogram is shown in panel (a) for particles that have drifted shoreward by at least 3 km, binned in 1 km intervals. Panel (b) presents a heatmap of the distance travelled by those particles, where colored bins indicate the average horizontal distance traveled by particles initially seeded at each corresponding location. In panel (c), the combined CDF and histogram represent particles that have entered the core, along with their corresponding residence times. Finally, panel (d) shows the associated heatmap of particles' residence time.

classified as entrained if, at any point in its trajectory, its horizontal velocity in a wave-attached reference frame reaches $-0.01\ m/s$. This threshold corresponds to nearly the propagation speed of the ISW (see Fig. 7), which a particle can attain only upon entrainment. The particle detrainment time is defined as the last instance its velocity falls below $-0.35\ m/s$, a threshold derived from the recirculating core velocities shown in Fig. 7. This value is further justified by the absence of such velocities outside the wave and by the sustained velocity oscillations around the ISW celerity observed in trapped particles (Figs. 7 and 8). Using this criterion, 42% of the particles with $\geq 3\ km$ of drift, amounting to 39,314, are classified as core residents.

Per Fig. 10c, the residence times span a wide range, and a distinct peak between 120 and 140 minutes is observed, suggesting that a large portion of particles remain inside the ISW for at least two hours. However, one should emphasize that these durations do

not necessarily account for the time of detrainment, as the finite simulation time limits the observation of the full residence history. By the final timestep, about 50% of the entrained particles have reached velocities below $-0.035\ m/s$ and are thus considered to be in the process of detrainment. Although Fig. 9b shows that approximately 35,000 particles are located within the wave's interior, a substantial fraction of them appear to be exiting the recirculating core.

The CDF in Fig. 10c rises steeply within the first 150 minutes, showing that over 60% of particles classified as residents exhibit residence times of at least two and a half hours. Beyond this point, the curve gradually flattens, indicating that a smaller yet non-negligible fraction remain inside the ISW for substantially longer. The long tail, in conjunction with the secondary histogram peak near 210 minutes, suggests a subset of particles that become deeply embedded in the core's recirculating structure and are retained over extended durations. This behavior underscores the ISW's capacity to act as an efficient transport vehicle. Nevertheless, the finite simulation duration limits these conclusions: for particles entrained at later stages, the available data may underestimate their residence times, leaving open the possibility that many would have remained trapped for even longer distances had the simulation continued.

Panel (d) of Fig. 10 displays a heatmap of the mean duration of particles' residence time, binned according to their initial positions in the domain. Note that, the averaging shown here is applied only to the subset of particles previously identified as entrained, and therefore, the color scale is not directly comparable to that of panel (b), which includes all particles with shoreward drift $\geq 3\ km$. Although the number of particles entrained from the deeper portion of the water column is relatively low (e.g. isolated red bins at 17–19 m depth near 37 km along the transect), those that were entrained exhibit prolonged residence times, highlighting the efficiency of the ISW in retaining particles from this region once entrained.

The spatial structure of the heatmap in panel (d) closely mirrors the large-drift regions in panel (b), revealing distinct zones of entrainment linked to extended residence times within the ISW core. Particles initially located between 40–43 km along the transect exhibit the longest average residence times, approaching 5 hours. The region spanning 50–58km horizontally and 15.5–19 m in depth shows the highest concentration of entrained particles, corresponding to the peak of resident-entrainment activity. This zone aligns with the portion of the wave undergoing the most vigorous convective plunge as it shoals over the steepest bathymetric slope. In contrast, particles seeded both earlier and later in the simulation exhibit weaker spatial coherence and are more vertically confined, particularly during the earlier stages of wave propagation.

As shown in panel (d), the initial vertical positions of the entrained particles span $[15, 20]$ m, while their final positions upon detrainment (not explicitly shown) lie within $[12.5, 16.5]$ m, consistent with the detrainment channel identified in Fig. 9a. Most particles experience a cumulative vertical displacement of ≤ 1 m. To quantify this, the vertical displacement distribution was computed for all particles located outside the ISW at both the initial and final snapshots (not explicitly shown), but which were entrained at least once during the simulation. The resulting histogram exhibits a slightly skewed Gaussian-like shape, with a mean displacement of -0.64 m, standard deviation of 1.09 m, and median of -0.43 m. These small differences between entrainment and detrainment depths suggest the potential for modest but non-negligible diapycnal mixing (Carter et al. 2005; Jones et al. 2020) in the ISW wake.

4 Concluding Remarks

A detailed Lagrangian and Eulerian analysis is presented for a single, two-dimensional ISW shoaling over a gentle slope in the SCS, and its interaction with ambient neutrally buoyant particles. A key dynamic feature is the baroclinic generation of negative

(counter-clockwise) vorticity at the wave rear, which intensifies during the onset of convective instability due to the rear-steepening of lighter isopycnals above the symmetric waveform (here, the pycnocline). A combination of generated and advected vorticity, in conjunction with the classical ISW-induced circulation of fluid entering from the front, wrapping around the depression, and exiting at the rear, facilitates the formation of a pair of counter-rotating vortices that evolve into a persistently identifiable subsurface core. A thin, tendril-like layer of negative vorticity also forms at the interface between these vortices, extending from the wave's trailing edge toward the core, and plays a central role in mediating particle entrainment and detrainment.

Particle entrainment is initially driven by the rear-side vorticity tendril, forming a tongue-like structure that draws particles into the wave. As the ISW shoals towards the steepest slope of the simulated transect and convective instability amplifies, additional vigorous entrainment occurs due to the plunging of heavier isopycnals. In later stages, weaker entrainment also takes place from the top and bottom of the core. Throughout the evolution, all entrained particles originate from a vertically-narrow band situated just above the pycnocline, suggesting that Lagrangian observational instruments have to be deployed precisely within this band to be entrained by the ISW. Once entrained, particle trajectories reveal intense stirring within the wave interior, especially in regions where smaller and less coherent vortices dominate. Detrainment pathways are more confined and primarily guided by the evolving vorticity tendril, while suggesting a potential for limited diapycnal mixing, although its quantification was beyond the scope of this study.

The simulation reveals substantial shoreward transport, with entrained particles exhibiting horizontal displacements exceeding 35 km and residence times longer than 4 hours. These findings highlight the capacity of ISWs to facilitate long-distance particle transport and material redistribution in the ocean interior.

Though not shown, comparisons with the y-averaged velocity field from fully three-dimensional simulations (Bolioudakis et al. 2025) reveal qualitative agreement in the streamline structure during the formation and evolution of the ISW core, particularly in cases without Kelvin–Helmholtz billows or a developed wake, thereby supporting the relevance of the two-dimensional results. These results provide a foundation for future turbulence-resolving, three-dimensional simulations with embedded particle tracking. The role of convectively-driven turbulence in further facilitating particle entrainment/detrainment, by creating additional pathways while also enhancing particle mixing, remains an open question for future studies requiring computationally-demanding high-resolution simulations. A related question concerns the ensuing shear instability, reproducible only in three dimensions (see Bolioudakis et al. (2025) Appendix B), and the contribution of turbulence generated by large-scale Kelvin–Helmholtz billows at the resulting wake.

Supplementary information. The online version includes one supplementary animation showing the wave's evolution in three panels (top to bottom): density (σ) contours, vorticity (ω_y) contours (both in a wave-following frame), and the wave-trough position in a fixed frame. Two particle sets are superimposed: a single set released within the wave core (magenta), and continuous releases near the pycnocline (plotted in black; only particles advected ≥ 10 km are shown).

Acknowledgements. The authors are grateful to Professor Alejandro Orfila for inspiring discussions and guidance on Lagrangian Coherent Structures techniques. They also thank Dr. Thomas J. Farrar for the helpful and constructive feedback during the critical stages of the present study. Dr. Theodoros Diamantopoulos and Dr. Bjorn Klose made important contributions in the early stages of flow-solver/particle-tracker coupling. Lastly, the authors acknowledge the Ocean Physics and Modeling Group at the University of Athens, and particularly Professor Sarantis Sofianos, for their warm hospitality during the final stages of writing this manuscript.

Declarations

Funding This research did not receive any specific grant from funding agencies in the public, commercial, or not-for-profit sectors.

Competing interests The authors declare no competing interests.

Consent for publication Consent for publication is approved by all the authors.

Data availability Data required to guide the main analysis and figures contained in this manuscript are available by request.

Author contribution TB: conceptualization, methodology, software implementation, simulations, formal analysis, writing-original draft. GT: software implementation, methodology, writing-original draft. PJD: supervision, conceptualization, methodology, writing-original draft. RCL: conceptualization, methodology. KL: conceptualization, methodology. JW: software implementation. GJ: methodology, software implementation. All authors contributed to the interpretation of results, discussion of the associated dynamics, and revision of the manuscript.

Appendix A Computational Tool

A.1 Flow Solver

This study leverages a hybrid Nodal Spectral Element/Fourier Galerkin Method (hereafter referred to as the *flow solver*) for the incompressible Navier–Stokes equations under the Boussinesq approximation, formulated for long, potentially deformed, doubly non-periodic domains (Diamantopoulos et al. 2022). For the bathymetric transect shown in Fig. 1a, two-dimensional simulations are conducted on a vertical plane oriented normal to the isobaths. The numerical tool, by employing a fast hybrid direct/iterative solver for the 2D pressure Poisson equation (Karniadakis and Sherwin 2005; Joshi et al. 2016; Diamantopoulos et al. 2022), is specifically designed to model and

efficiently resolve the propagation of nonlinear, nonhydrostatic internal waves and the instability-driven evolution of any finer-scale motions therein.

Numerical stability of the flow solver is maintained through the application of an explicit spectral filter of 14^{th}-order exponential form (Diamessis et al. 2005), equivalent to the use of hyperviscous operators (Boyd 1998; Gottlieb and Hesthaven 2001). Polynomial dealiasing is additionally applied to the nonlinear and advective terms (Kirby and Karniadakis 2003; Malm et al. 2013; Diamantopoulos et al. 2022). Lastly, identical to Bolioudakis et al. (2025), an artificial Rayleigh-type damping layer is imposed at the left and right boundaries of the domain to suppress any potential spurious wave reflection (Rivera-Rosario et al. 2020).

A.2 Particle Tracker

The simulations presented here build upon the one-way online coupling of the previously described flow solver with the high-accuracy parallel particle tracking scheme used in Klose et al. (2020) (hereafter referred to as the *particle tracker*). Specifically, the parallel, element-based particle tracking algorithm described in detail by Mittal et al. (2019) is employed. This algorithm is optimized for non-uniform, non-equispaced elemental grids, such as those used in spectral element methods, where numerical solutions are computed at Gauss–Lobatto–Legendre quadrature points (Noorani et al. 2015), and leverages the fast and robust interpolation capabilities of the *gslib* library (Lottes and Offermans 2017).

A.3 Particle Tracker Solver Coupling

The particle tracker is designed to execute as in multiple process, multiple data (MPMD) message passing interface (MPI) configuration where both the flow solver and the tracker execute concurrently. Non-inertial particles do not require two-way coupling with the flow, admitting flexibility in its execution. The tracker was designed

with this in mind so that it could be applied to a large variety of problems through coupling with different flow solvers, incurring minimal execution overhead.

Once the flow solver and particle tracker's initialization are complete, only the solver's current time step and flow field need to be transmitted to the particle tracker before the solver can continue to its next time step, proceeding in a lagged, lock-step manner. Provided sufficient computational cores are available, this allows particle tracking execution to be overlapped with the flow solver's. Since the flow solver is significantly more computationally expensive than particle advection, the particle tracking is usually completely overlapped with the flow solver and is effectively free.

The particle tracker interpolates the solver's velocity fields at each particle location using an eighth-order Lagrange interpolation scheme, solving two initial-value problems of the form $\dot{x}_p(t) = u(x_p(t), t)$, one for each spatial component for every particle's position. Particles are advanced to their new positions using a third-order Adams-Bashforth time integration method.

A.4 Computational resources

Both simulations were conducted on the group's 28-core Intel Xeon E5-2680v4 (Broadwell architecture) system with hyperthreading enabled. The particle tracker is decoupled from the flow solver and executes in a multiple program, multiple data (MPMD) configuration with 16 cores allocated to the flow solver and 8 cores to the particle tracker. The total wall-clock time required for the simulations presented here was 28 days.

Appendix B FTLE Computation

As the ISW shoals within each overlapping window, particle trajectories (of Simulation B; see 2.4) are tracked at every time step over a finite-time integration interval. These trajectories define the flow map $\mathbf{\Phi}$, which advances particles from their initial positions

($\mathbf{x}_i$; Eq. (B1) to their final positions ($\mathbf{x}_f$; Eq. (B2) after a finite time interval (Shadden et al. 2005).

The particles are initially positioned on the structured grid of the flow solver. For each interior (non-boundary) particle, spatial derivatives are approximated using centered finite differences based on the positions of neighboring particles in the grid. These local finite differences in particle displacement (representing implicit local relative separations) are then used to construct the deformation gradient tensor $\mathbf{D\Phi}$ (Eq. B3), i.e., the spatial gradient of the flow map evaluated at each interior point on the initial grid. The corresponding Cauchy–Green strain tensor $\mathbf{C}$ is then computed as shown in Eq.(B4). Finally, the largest eigenvalue of the Cauchy–Green tensor (the leading Lyapunov exponent), denoted by $\lambda_{\max}$, is used to calculate the forward-in-time Finite-Time Lyapunov Exponent (FTLE) field, F_{FTLE}.

$$\mathbf{x}_0(t_0) = \begin{bmatrix} x_1(t_0) & z_1(t_0) \\ x_2(t_0) & z_2(t_0) \\ \vdots & \vdots \\ x_N(t_0) & z_N(t_0) \end{bmatrix}, \tag{B1}$$

$$\mathbf{x_f}(t_0+T) = \begin{bmatrix} x_1(t_0+T) & z_1(t_0+T) \\ x_2(t_0+T) & z_2(t_0+T) \\ \vdots & \vdots \\ x_N(t_0+T) & z_N(t_0+T) \end{bmatrix}. \tag{B2}$$

$$D\Phi = \begin{bmatrix} \frac{\partial x(t_0+T)}{\partial x_0} & \frac{\partial x(t_0+T)}{\partial z_0} \\ \frac{\partial y(t_0+T)}{\partial x_0} & \frac{\partial z(t_0+T)}{\partial z_0} \end{bmatrix} \approx \begin{bmatrix} \frac{\Delta x(T)}{\Delta x_0} & \frac{\Delta x(T)}{\Delta z_0} \\ \frac{\Delta z(T)}{\Delta x_0} & \frac{\Delta z(T)}{\Delta z_0} \end{bmatrix}, \tag{B3}$$

$$\mathbf{C}(t_0, T, \mathbf{x}_0) = D\Phi^T(t_0, T, \mathbf{x}_0) \cdot D\Phi(t_0, T, \mathbf{x}_0), \tag{B4}$$

$$F_{FTLE}(t_0, T, \mathbf{x}_0) = \frac{1}{|T|} \ln \sqrt{\lambda_{\max}\left(\mathbf{C}(t_0, T, \mathbf{x}_0)\right)}, \tag{B5}$$

The theoretical formulation of the backward-in-time FTLE requires reinitializing particles throughout the domain at the final state of the solution; that is, when the ISW has propagated far enough to reach the end-time (near the right boundary) of the overlapping computational window. These particles would then be advected backward in time, and the FTLE procedure will be identical to the forward-time case, with the initial and final positions reversed. However, this approach is not feasible in the present simulations due to two primary limitations. First, the velocity field computed by the flow solver at each grid point is not stored at every time step, so particles cannot be advected in post-processing mode; only particle coordinates are retained. Second, reinitializing the ISW at the right boundary and forcing it to propagate backward would not reproduce the exact time-reversed flow, due to two main reasons. First, forcing the wave to travel backward in time with $C = -C_{\text{prop}}$ is nontrivial, especially for waves shoaling over varying bathymetry. Furthermore, the application of the spectral filter, as outlined in App. A.1, introduces numerical dissipation that renders the flow evolution inherently irreversible. Consequently, to construct the backward FTLE flow map, we follow the approach of Nelson and Jacobs (2015), which approximates the backward-time FTLE (B_{FTLE}) by integrating the available flow map from $t_0 + T$ back to t_0.

References

Aigner, A., Broutman, D., Grimshaw, R.: Numerical simulations of internal solitary waves with vortex cores. Fluid Dyn. Res. **25**(6), 315 (1999) https://doi.org/10.1016/S0169-5983(98)00046-X

Arthur, R.S., Fringer, O.B.: Transport by breaking internal gravity waves on slopes. Journal of Fluid Mechanics **789**, 93–126 (2016) https://doi.org/10.1017/jfm.2015.723

Alford, M.H., Peacock, T., MacKinnon, J.A., Nash, J.D., Buijsman, M.C., Centurioni, L.R., Chao, S.-Y., Chang, M.-H., Farmer, D.M., Fringer, O.B., Fu, K.-H., Gallacher, P.C., Graber, H.C., Helfrich, K.R., Jachec, S.M., Jackson, C.R., Klymak, J.M., Ko, D.S., Jan, S., Johnston, T.M.S., Legg, S., Lee, I.-H., Lien, R.-C., Mercier, M.J., Moum, J.N., Musgrave, R., Park, J.-H., Pickering, A.I., Pinkel, R., Rainville, L., Ramp, S.R., Rudnick, D.L., Sarkar, S., Scotti, A., Simmons, H.L., St. Laurent, L.C., Venayagamoorty, S.K., Wang, Y.-H., Wang, J., Yang, Y.-J., Paluszkiewicz, T., Tang, T.-Y.: The formation and fate of internal waves in the South China Sea. Nature **521**, 65–69 (2015) https://doi.org/10.1038/nature14399

Aref, H.: Stirring by chaotic advection. Journal of Fluid Mechanics **143**, 1–21 (1984) https://doi.org/10.1017/S0022112084001233

Bolioudakis, T., Diamantopoulos, T., Diamessis, P.J., Lien, R.-C., Lamb, K.G., Rivera-Rosario, G., Thomsen, G.N.: Formation and evolution of turbulence in convectively unstable internal solitary waves of depression shoaling over gentle slopes in the South China Sea. arXiv preprint arXiv:2502.01607 (2025)

Boyd, J.P.: Two comments on filtering (artificial viscosity) for Chebyshev and Legendre spectral and spectral element methods: Preserving boundary conditions and interpretation of the filter as a diffusion. J. Comput. Phys. **143**(1), 283–288 (1998) https://doi.org/10.1006/jcph.1998.5961

Cheng, Y.-H., Chang, M.-H., Yang, Y.J., Jan, S., Ramp, S.R., Davis, K.A., Reeder, D.B.: Insights into internal solitary waves east of Dongsha Atoll from integrating geostationary satellite and mooring observations. J. Geophys. Res. **129**(8) (2024) https://doi.org/10.1029/2024JC021109

Carr, M., Davies, P.: Experimental evidence of internal solitary wave-induced global instability in shallow water benthic boundary layers. Physics of Fluids **20** (2008)

https://doi.org/10.1063/1.2931693

Carter, G.S., Gregg, M.C., Lien, R.-C.: Internal waves, solitary-like waves, and mixing on the Monterey Bay shelf. Cont. Shelf Res. **25**(12), 1499–1520 (2005) https://doi.org/10.1016/j.csr.2005.04.011

Canuto, C., Hussaini, M.Y., Quarteroni, A., Zang, T.A.: Spectral Methods: Evolution to Complex Geometries and Applications to Fluid Dynamics. Scientific Computation. Springer, Berlin, Heidelberg (2007). https://doi.org/10.1007/978-3-540-30728-0

Chang, M.-H., Lien, R.-C., Lamb, K., Diamessis, P.: Long-term observations of shoaling internal solitary waves in the Northern South China Sea. J. Geophys. Res.: Oceans **126** (2021) https://doi.org/10.1029/2020JC017129

D'Asaro, E.A.: Performance of autonomous lagrangian floats. Journal of Atmospheric and Oceanic Technology **20**(6), 896–911 (2003) https://doi.org/10.1175/1520-0426(2003)020⟨0896:POALF⟩2.0.CO;2

Davis, K.A., Arthur, R.S., Reid, E.C., Rogers, J.S., Fringer, O.B., Decarlo, T.M., Cohen, A.L.: Fate of internal waves on a shallow shelf. J. Geophys. Res.: Oceans **125**(5) (2020) https://doi.org/10.1029/2019JC015377

Diamessis, P., Domaradzki, J., Hesthaven, J.: A spectral multidomain penalty method model for the simulation of high Reynolds number localized stratified turbulence. J. Comput. Phys. **202**, 298–322 (2005) https://doi.org/10.1016/j.jcp.2004.07.007

D'Ovidio, F., Isern-Fontanet, J., López, C., Hernández-García, E., García-Ladona, E.: Comparison between Eulerian diagnostics and finite-size Lyapunov exponents computed from altimetry in the Algerian basin. Deep Sea Research Part I: Oceanographic Research Papers **56**(1), 15–31 (2009) https://doi.org/10.1016/j.dsr.2008.07.

014

Diamantopoulos, T., Joshi, S., Thomsen, G., Rivera-Rosario, G., Diamessis, P., Rowe, K.: A high accuracy/resolution spectral element/Fourier-Galerkin method for the simulation of shoaling non-linear internal waves and turbulence in long domains with variable bathymetry. Ocean Model **176**, 102065 (2022) https://doi.org/10.1016/j.ocemod.2022.102065

Davis, K.A., Monismith, S.G.: The modification of bottom boundary layer turbulence and mixing by internal waves shoaling on a barrier reef. Journal of Physical Oceanography **41**(11), 2223–2241 (2011) https://doi.org/10.1175/2011JPO4344.1

Deepwell, D., Sapède, R., Buchart, L., Swaters, G.E., Sutherland, B.R.: Particle transport and resuspension by shoaling internal solitary waves. Physical Review Fluids **5**(5), 054303 (2020) https://doi.org/10.1103/PhysRevFluids.5.054303

Dunphy, M., Subich, C., Stastna, M.: Spectral methods for internal waves: indistinguishable density profiles and double-humped solitary waves. Nonlinear Proc. Geoph. **18**, 351–358 (2011) https://doi.org/10.5194/npg-18-351-2011

Gottlieb, D., Hesthaven, J.S.: Spectral methods for hyperbolic problems. J. Comp. Appl. Math. **128**(1), 83–131 (2001) https://doi.org/10.1016/bs.hna.2016.09.007 . Numerical Analysis 2000. Vol. VII: Partial Differential Equations

Gil, G.T.C.: Mass Transport and Shear-Flow Dispersion Due to Nonlinear Internal Gravity Waves

Garwood, J.C., Lucas, A.J., Naughton, P., Alford, M.H., Roberts, P.L.D., Jaffe, J.S., Degelleke, L., Franks, P.J.S.: A novel cross-shore transport mechanism revealed by subsurface, robotic larval mimics: Internal wave deformation of the background velocity field. Limnology and Oceanography **65**(7), 1456–1470 (2020) https://doi.

org/10.1002/lno.11400

Garwood, J.C., Musgrave, R.C., Lucas, A.J.: Life in internal waves. Oceanography **33**(3), 38–49 (2020) https://doi.org/10.5670/oceanog.2020.313

Girton, J.B., Whalen, C.B., Lien, R.-C., Kunze, E.: Coherent float arrays for near-inertial wave studies. Oceanography **37**(4), 58–67 (2024) https://doi.org/10.5670/oceanog.2024.306

Guo, D., Zhan, P., Hoteit, I.: Three-dimensional simulation of shoaling internal solitary waves and their influence on particle transport in the southern Red Sea. Journal of Geophysical Research: Oceans **126**(4), 2020–016335 (2021) https://doi.org/10.1029/2020JC016335

Haller, G.: Lagrangian coherent structures from approximate velocity data. Physics of Fluids **14**(6), 1851–1861 (2002) https://doi.org/10.1063/1.1477449

Haller, G.: Lagrangian coherent structures. Annual Review of Fluid Mechanics **47**, 137–162 (2015) https://doi.org/10.1146/annurev-fluid-010313-141322

Henderson, S.M.: Upslope internal-wave Stokes drift, and compensating downslope Eulerian mean currents, observed above a lakebed. Journal of Physical Oceanography **46**(6), 1947–1961 (2016) https://doi.org/10.1175/JPO-D-15-0114.1

He, Y., Lamb, K.G., Lien, R.-C.: Internal solitary waves with subsurface cores. J. Fluid Mech. **873**, 1–17 (2019) https://doi.org/10.1017/jfm.2019.407

Helfrich, K.R., Melville, W.K.: Long nonlinear internal waves. Annu. Rev. Fluid Mech. **38**, 395–425 (2006) https://doi.org/10.1146/annurev.fluid.38.050304.092129

Ide, K., Small, D., Wiggins, S.: Distinguished hyperbolic trajectories in time-dependent fluid flows: Analytical and computational approach for velocity fields defined as data

sets. Nonlinear Processes in Geophysics **9**(3/4), 237–263 (2002) https://doi.org/10.5194/npg-9-237-2002

Jones, N., Ivey, G., Rayson, M., Kelly, S.: Mixing driven by breaking nonlinear internal waves. Geophysical Research Letters **47** (2020) https://doi.org/10.1029/2020GL089591

Jackson, C.R., Silva, J.C.B.D., Jeans, G.: The generation of nonlinear internal waves. Oceanography **25** (2012) https://doi.org/10.5670/oceanog.2012.46

Joshi, S.M., Thomsen, G., Diamessis, P.J.: Deflation-accelerated preconditioning of the Poisson–Neumann Schur problem on long domains with a high-order discontinuous element-based collocation method. J. Comput. Phys. **313**(209-232) (2016) https://doi.org/10.1016/j.jcp.2016.02.033

Kramer, W., Clercx, H.J.H., Heijst, G.J.F.: Vorticity dynamics of a dipole colliding with a no-slip wall. Physics of Fluids **19**(12), 126603 (2007) https://doi.org/10.1063/1.2814345

Karniadakis, G.E., Israeli, M., Orszag, S.A.: High-order splitting methods for the incompressible Navier-Stokes equations. J. Comput. Phys. **97**, 411–443 (1991) https://doi.org/10.1016/0021-9991(91)90007-8

Klose, B.F., Jacobs, G.B., Serra, M.: Kinematics of Lagrangian flow separation in external aerodynamics. AIAA Journal **58**(5), 1926–1938 (2020) https://doi.org/10.2514/1.J059026

Kirby, R., Karniadakis, G.: De-aliasing on non-uniform grids: Algorithms and applications. J. Comput. Phys. **191**, 249–264 (2003) https://doi.org/10.1016/S0021-9991(03)00314-0

Klymak, J.M., Moum, J.N.: Internal solitary waves of elevation advancing on a shoaling shelf. Geophys. Res. Lett. **30**(20) (2003) https://doi.org/10.1029/2003GL017706 . 2045

Karniadakis, G., Sherwin, S.: Spectral/HP Element Methods for Computational Fluid Dynamics, (2005). https://doi.org/10.1093/acprof:oso/9780198528692.001.0001

Lamb, K.G.: Particle transport by nonbreaking, solitary internal waves. J. Geophys. Res. **102**(C8), 18641–18660 (1997)

Lamb, K.G.: A numerical investigation of solitary internal waves with trapped cores formed via shoaling. J. Fluid Mech. **451**, 109–144 (2002) https://doi.org/10.1017/S002211200100636X

Lamb, K.G.: Shoaling solitary internal waves: on a criterion for the formation of waves with trapped cores. J. Fluid Mech. **478**, 81–100 (2003) https://doi.org/10.1017/S0022112002003269

Lien, R.-C., D'Asaro, E.A., Henyey, F., Chang, M.-H., Tang, T.-Y., Yang, Y.-J.: Trapped core formation within a shoaling nonlinear internal wave. J. Phys. Oceanogr. **42**, 511–525 (2012) https://doi.org/10.1175/2011JPO4578.1

Lien, R.-C., D'Asaro, E.A., Mcphaden, M.J.: Internal waves and turbulence in the upper central equatorial pacific: Lagrangian and Eulerian observations. Journal of Physical Oceanography **32**(9), 2619–2639 (2002) https://doi.org/10.1175/1520-0485(2002)032⟨2619:IWATIT⟩2.0.CO;2

Luzzatto-Fegiz, P., Helfrich, K.R.: Laboratory experiments and simulations for solitary internal waves with trapped cores. J. Fluid Mech. **757**, 354–380 (2014)

Lien, R.-C., Henyey, F., Ma, B., Yang, Y.-J.: Large-amplitude internal solitary waves

observed in the northern South China Sea: Properties and energetics. J. Phys. Oceanogr. **44**(4), 1095–1115 (2014) https://doi.org/10.1175/JPO-D-13-088.1

Lamb, K.G., Lien, R.-C., Diamessis, P.J.: Internal solitary waves and mixing. In: Cochran, J.K., Bokuniewicz, H.J., Yager, P.L. (eds.) Encyclopedia of Ocean Sciences (Third Edition), Third edition edn., pp. 533–541. Academic Press, Oxford (2019). https://doi.org/10.1016/B978-0-12-409548-9.10951-0

Lottes, J., Offermans, N.: Gather-scatter library in nek5000. Technical report, KTH Royal Institute of Technology (2017). Documentation of the gs library developed by James Lottes

Long, R.R.: Some aspects of the flow of stratified fluids i. a theoretical investigation. Tellus **8**, 460–471 (1953) https://doi.org/10.1111/j.2153-3490.1955.tb01171.x

Lucas, A.J., Pinkel, R.: Observations of coherent transverse wakes in shoaling nonlinear internal waves. J. Phys. Oceanogr. **52**(6) (2022) https://doi.org/10.1175/JPO-D-21-0059.1

Lamb, K.G., Warn-Varnas, A.: Two-dimensional numerical simulations of shoaling internal solitary waves at the ASIAEX site in the South China Sea. Nonlinear Proc. Geoph. **22**, 289–312 (2015) https://doi.org/10.5194/npg-22-289-2015

Lien, R.-C., Yang, T.Y., Chang, M.H., D'Asaro, E.A.: Energy of nonlinear internal waves in the South China Sea. Geophys. Res. Lett. **32**(L05615) (2005) https://doi.org/10.1029/2004GL022012

Mittal, K., Dutta, S., Fischer, P.: Nonconforming Schwarz-spectral element methods for incompressible flow. Computers & Fluids **191**, 104237 (2019) https://doi.org/10.1016/j.compfluid.2019.104237

Moum, J.N., Farmer, D.M., Smyth, W.D., Armi, L., Vagle, S.: Structure and generation of turbulence at interfaces strained by internal solitary waves propagating shoreward over the continental shelf. J. Phys. Oceanogr. **33**, 2093–2112 (2003)

Moum, J.N., Farmer, D.M., Shroyer, E.L., Smyth, W.D., Armi, L.a.: Dissipative losses in nonlinear internal waves propagating across the continental shelf. J. Phys. Oceanogr. **37**(7), 1989–1995 (2007) https://doi.org/10.1175/JPO3091.1

Moore, S.E., Lien, R.-C.: Pilot whales follow internal solitary waves in the South China Sea. Mar. Mammal Sci. **21**(1), 193–196 (2007) https://doi.org/10.1111/j.1748-7692.2006.00086.x

Malm, J., Schlatter, P., Fischer, P., Henningson, D.: Stabilization of the spectral element method in convection dominated flows by recovery of skew-symmetry. J. Sci. Comput. **57** (2013) https://doi.org/10.1007/s10915-013-9704-1

Nielson, J.R., Henderson, S.M.: Bottom boundary layer mixing processes across internal seiche cycles: Dominance of downslope flows. Limnology and Oceanography **67**(5), 1111–1125 https://doi.org/10.1002/lno.12060

Nelson, D.A., Jacobs, G.B.: DG-FTLE: Lagrangian coherent structures with high-order discontinuous-Galerkin methods. J. Comput. Phys. **295**, 65–86 (2015)

Noorani, A., Peplinski, A., Schlatter, P.: Informal introduction to program structure of spectral interpolation in nek5000. Technical report, KTH Royal Institute of Technology (2015)

Reid, E.C., Decarlo, T.M., Cohen, A.L., Wong, G.T.F., Lentz, S.J., Safaie, A., Hall, A., Davis, K.A.: Internal waves influence the thermal and nutrient environment on a shallow coral reef. Limnology and Oceanography **64**(5), 1949–1965 (2019) https://doi.org/10.1002/lno.11162

Rouvinskaya, E., Kurkina, O., Kurkin, A., Giniyatullin, A.: Transfer of particles during the propagation of internal waves in the Baltic sea. In: 2018 IEEE/OES Baltic International Symposium (BALTIC), pp. 1–5 (2018). https://doi.org/10.1109/BALTIC.2018.8425593 . IEEE

Rivera-Rosario, G., Diamessis, P.J., Lien, R.-C., Lamb, K.G., Thomsen, G.N.: Formation of Recirculating Cores in Convectively Breaking Internal Solitary Waves of Depression Shoaling over Gentle Slopes in the South China Sea. J. Phys. Oceanogr. **50**(5), 1137–1157 (2020) https://doi.org/10.1175/JPO-D-19-0036.1

Rivera-Rosario, G., Diamessis, P., Lien, R.-C., Lamb, K., Thomsen, G.: Three-dimensional perspective on a convective instability and transition to turbulence in an internal solitary wave of depression shoaling over gentle slopes. Env. Fluid Mech. (2022) https://doi.org/10.1007/s10652-022-09844-7

Shadden, S.C., Dabiri, J.O., Marsden, J.E.: Lagrangian analysis of fluid transport in empirical vortex ring flows. Physics of Fluids **18**(4), 047105 (2006) https://doi.org/10.1063/1.2189885

Sandstrom, H., Elliott, J.A.: Internal tide and solitons on the Scotian shelf: A nutrient pump at work. J. Geophys. Res. **89**(C4), 6415–6426 (1984) https://doi.org/10.1029/JC089iC04p06415

Salloum, M., Knio, O., Brandt, A.: Numerical simulation of mass transport in internal solitary waves. Physics of Fluids **24** (2012) https://doi.org/10.1063/1.3676771

Steinbuck, J.V., Koseff, J.R., Genin, A., Stacey, M.T., Monismith, S.G.: Horizontal dispersion of ocean tracers in internal wave shear. Journal of Geophysical Research: Oceans **116**(C11), 11021 (2011) https://doi.org/10.1029/2011JC007213

St. Laurent, L.: Turbulent dissipation on the margins of the South China Sea. Geophys.

Res. Lett. **35**(23) (2008) https://doi.org/10.1029/2008GL035520

Shadden, S.C., Lekien, F., Marsden, J.E.: Definition and properties of Lagrangian coherent structures from finite-time Lyapunov exponents in two-dimensional aperiodic flows. Physica D: Nonlinear Phenomena **212**(3), 271–304 (2005) https://doi.org/10.1016/j.physd.2005.10.007

Shanks, A.L., Morgan, S.G., MacMahan, J., Reniers, A.J.H.M., Jarvis, M., Brown, J., Fujimura, A., Griesemer, C.: Onshore transport of plankton by internal tides and upwelling-relaxation events. Marine Ecology Progress Series **502**, 39–51 (2014) https://doi.org/10.3354/meps10717

Shroyer, E.L., Moum, J.N., Nash, J.D.: Energy transformations and dissipation of nonlinear internal waves over New Jersey's continental shelf. Nonlinear Proc. Geoph. **17**(4), 345–360 (2010) https://doi.org/10.5194/npg-17-345-2010

Shroyer, E.L., Moum, J.N., Nash, J.D.: Nonlinear internal waves over New Jersey's continental shelf. J. Geophys. Res. **116**(C03022) (2011) https://doi.org/10.1029/2010JC006332

Scotti, A., Pineda, J.: Observation of very large and steep internal waves of elevation near the Massachusetts coast. Geophys. Res. Lett. **31**(22) (2004) https://doi.org/10.1029/2004GL021052 . L22307

Stastna, M., Poulin, F.J., Subich, C., Mecking, J.V.: The effect of stochastic perturbations on plankton transport by internal solitary waves. Nonlinear Processes in Geophysics **18**(6), 1001–1012 (2011) https://doi.org/10.5194/npg-18-1001-2011

Safaie, A., Silbiger, N.J., Mcclanahan, T.R., Pawlak, G., Barshis, D.J., Hench, J.L., Rogers, J.S., Williams, G.J., Davis, K.A.: High frequency temperature variability reduces the risk of coral bleaching. Nature Communications **9**(1), 1671 (2018) https:

//doi.org/10.1038/s41467-018-04074-2

Stastna, M.: Internal Waves in the Ocean: Theory and Practice. Springer, Cham, Switzerland (2022). https://doi.org/10.1007/978-3-030-99210-1

Strogatz, S.H.: Nonlinear Dynamics and Chaos: With Applications to Physics, Biology, Chemistry, and Engineering, 2nd edn. CRC Press, Boca Raton, FL (2018)

Sutherland, B.: Internal Gravity Waves. Cambridge University Press, Cambridge, UK (2010)

Stashchuk, N., Vlasenko, V.: Internal wave dynamics over isolated seamount and its influence on coral larvae dispersion. Frontiers in Marine Science **8**, 735358 (2021) https://doi.org/10.3389/fmars.2021.735358

Støylen, E., Weber, J.E.H.: Mass transport induced by internal Kelvin waves beneath shore-fast ice. Journal of Geophysical Research: Oceans **115**(C3) (2010) https://doi.org/10.1029/2009JC005298

Turkington, B., Eydel, , A., Wang, S.: A computational method for solitary internal waves in a continously stratified fluid. Stud. Appl. Math. **85**, 93–127 (1991) https://doi.org/10.1002/sapm199185293

Umeyama, M., Matsuki, S.: Measurements of velocity and trajectory of water particle for internal waves in two density layers. Geophysical Research Letters **38**(3), 03612 (2011) https://doi.org/10.1029/2010GL046419

Vieira, G.S., Allshouse, M.R.: Internal wave boluses as coherent structures in a continuously stratified fluid. Journal of Fluid Mechanics **885**, 35 (2020) https://doi.org/10.1017/jfm.2019.993

Sebille, E., Griffies, S.M., Abernathey, R., Adams, T.P., Berloff, P., Biastoch, A.,

Blanke, B., Chassignet, E.P., Cheng, Y., Cotter, C.J., Deleersnijder, E., Döös, K., Drake, H.F., Drijfhout, S., Gary, S.F., Heemink, A.W., Kjellsson, J., Koszalka, I.M., Lange, M., Lique, C., Macgilchrist, G.A., Marsh, R., Mayorga Adame, C.G., Mcadam, R., Nencioli, F., Paris, C.B., Piggott, M.D., Polton, J.A., Rühs, S., Shah, S.H.A.M., Thomas, M.D., Wang, J., Wolfram, P.J., Zanna, L.: Lagrangian ocean analysis: Fundamentals and practices. Ocean Modelling **121**, 49–75 (2018) https://doi.org/10.1016/j.ocemod.2017.11.008

Wang, Y.-H., Dai, C.-F., Chen, Y.-Y.: Physical and ecological processes of internal waves on an isolated reef ecosystem in the South China Sea. Geophysical Research Letters **34**(18) (2007) https://doi.org/10.1029/2007GL030658

Zhang, S., Alford, M.H.: Instabilities in nonlinear internal waves on the Washington continental shelf. J. Geophys. Res. **120**, 5272–5283 (2015) https://doi.org/10.1002/2014JC010638

Zhou, Q., Diamessis, P.J.: Lagrangian flows within reflecting internal waves at a horizontal free-slip surface. Phys. Fluids **27**(12) (2015)

Zulberti, A., Jones, N.L., Ivey, G.N.: Observations of enhanced sediment transport by nonlinear internal waves. Geophys. Res. Lett. **47**(19) (2020) https://doi.org/10.1029/2020GL088499

Zhang, J., Zou, L., Sun, T., Ma, X., Wang, H.: Non-Boussinesq effect on the internal solitary wave propagation under a Lagrangian-like description for various pycnocline thickness conditions. Journal of Computational and Applied Mathematics **437**, 115648 (2024) https://doi.org/10.1016/j.cam.2023.115648

Supplementary Files

This is a list of supplementary files associated with this preprint. Click to download.

- ReadmeSupplementaryAnimationOcDynBolioudakis.pdf
- OcDynSupplementaryAnimationBolioudakisetal.mp4